

# The complex basal morphology and ice dynamics of Nansen Ice Shelf, East Antarctica

Christine F. Dow<sup>1</sup>, Derek Mueller<sup>2</sup>, Peter Wray<sup>1</sup>, Drew Friedrichs<sup>3,4</sup>, Alexander L. Forrest<sup>3,4</sup>, Jasmin B. McInerney<sup>3,4</sup>, Jamin Greenbaum<sup>5</sup>, Donald D. Blankenship<sup>6</sup>, Choon Ki Lee<sup>7</sup>, Won Sang Lee<sup>7</sup>

5

<sup>1</sup>Department of Geography and Environmental Management, University of Waterloo, Waterloo, Canada, N2L 3G1

<sup>2</sup>Department of Geography and Environmental Studies, Carleton University, Ottawa, Canada, K1S 5B6

<sup>3</sup>Department of Civil and Environmental Engineering, University of California – Davis, Davis, USA, 95616

<sup>4</sup>Tahoe Environmental Research Center, University of California – Davis, Incline Village, USA, 89451

10 <sup>5</sup>Scripps Institution of Oceanography, University of California, San Diego, La Jolla, CA, USA

<sup>6</sup>Institute for Geophysics, Jackson School of Geosciences, University of Texas at Austin, Austin, TX, USA, 78758

<sup>7</sup>Division of Glacial Environment Research, Korea Polar Research Institute, Incheon 21990, Republic of Korea

*Correspondence to:* Christine F. Dow (christine.dow@uwaterloo.ca)

**Abstract.** Ice shelf dynamics and morphology play an important role in the stability of floating bodies of ice by driving fracturing that can lead to calving, in turn impacting their ability of the ice shelf to buttress upstream grounded ice. Following a 2016 calving event at Nansen Ice Shelf, East Antarctica, we collected ~~We use a combination of~~ airborne and ground-based radar data and ~~ocean glider data to assess the drivers behind transverse fracture formation at this ice shelf. We combine these in situ data with published~~ satellite-derived data, ~~and oceanographic data collected at the Nansen Ice Shelf in East Antarctica~~ to examine the spatial variations in ice shelf draft, ~~the cause and effects of ice shelf strain rates, and~~ the role of a suture zone driving channelization of ocean water and resulting sub-ice shelf melt and freeze-on, and the cause and effects of ice shelf strain rates. We also use our in situ ~~the~~ datasets to assess limitations that may arise from relying on hydrostatic balance equations applied to ice surface elevation to determine ice draft morphology. We find that the Nansen Ice Shelf has a highly variable basal morphology driven primarily by the formation of basal fractures near the onset of floating ice convergence in the suture zone. This complex morphology is reflected in the ice shelf strain rates but not in the calculated hydrostatic balance thickness, which underestimates the scale of vertical and horizontal variability at the ice shelf base. The combination of thinner ice in the channelized suture zone, enhanced melt rates near the ice shelf terminus focussed in the steepest regions of the suture zone, and complex strain rates driven by ice dynamics and morphology have led to the formation of the fractures within the suture zone that have resulted in large-scale calving events. Similar transverse fractures at other Antarctic ice shelves may also be driven by ~~have~~ complex morphology, and predicting their formation and evolution could aid projections of ice shelf stability. ~~which is not fully reflected in satellite surface elevation data, yet may influence their stability.~~

15  
20  
25  
30

## 1 Introduction

Ice shelves buttress large portions of the Antarctic Ice Sheet, preventing destabilization of grounded ice and related discharge into the ocean (Dupont and Alley, 2005; Fürst et al., 2016; Scambos et al., 2014). The stability of these ice shelves is therefore vital for determining the future rise of global sea level. Fracturing and calving are key processes in the evolution of ice shelf morphology and its ability to hold back grounded ice. Ice shelf fractures occur in regions that are undergoing stress greater than the cohesive strength of the ice and can form or expand as a result of flexure (Vaughan et al., 2012); longitudinal stretching as ice moves beyond pinning points (Dow et al., 2018; Indrigo et al., 2020); advection of crevasses from grounded ice across the grounding line (Kulesa et al., 2014); and changes in buttressing causing ice shelf acceleration (Fürst et al., 2016). The primary controls of fracture formation include the ice thickness, the ice strain regime, and the ice rheology, along with additional factors such as the stress intensity factor (Lipovsky, 2018).

35  
40

It is possible to predict the response of a flat body of floating ice to warming atmospheric and ocean conditions but, in reality, ice shelves consist of complex morphology and rheology making it a challenge to determine potential fracture and/or break-up locations. The increasing availability of high-resolution data products such as ice velocity (e.g., Global Land Ice Velocity  
45 Extraction from Landsat 8 (GoLIVE) project, Scambos et al. (2016); and the Inter-Mission Time Series of Land Ice Velocity and Elevation (ITS\_LIVE) project, Gardner et al. (2020)), and ice surface elevation (e.g., the Reference Elevation Model of Antarctica (REMA, Howat et al., 2019)) opens up possibilities for large-scale spatial analyses of ice shelf processes. However, the use of inferred data (e.g., assumptions of hydrostatic equilibrium for floating ice bodies) may obfuscate ice shelf morphological details and lead to misconceptions regarding important processes and properties that could lead to fracturing.

50

~~Here we use~~ The Nansen Ice Shelf (NIS) in Terra Nova Bay underwent a large (213 km<sup>2</sup> in ice extent) calving event in 2016, driven by a transverse fracture that formed around 1987 in a thin suture zone in the centre of the ice shelf, which advected towards the shelf terminus while expanding laterally. Around the time of the calving event, a new fracture formed over the thinnest region of the central NIS (Dow et al., 2018). Both the initial location of the fractures and their rate of lateral expansion  
55 have been suggested to be linked to the presence of a basal channel thinning the suture zone, the thickness of the ice at the edge of the suture zone, and the ice surface strain patterns (Dow et al., 2018). Here, we investigate the conditions facilitating ice shelf fracture by analyzing ground-based and airborne ice-penetrating radar (IPR), and ice surface global positioning system (GPS) data that were collected around six months following the large calving event at NIS to assess ice shelf morphology and thinning rates. For our analysis we also utilize oceanographic data that were gathered under and in front of the NIS in 2019  
60 with an ocean glider system to determine if and where Ice Shelf Meltwater forms due to active basal melt. Finally, we use published satellite-derived digital elevation model (DEM), velocity, and basal melt products to examine the larger scale morphology of the NIS, calculate ice surface strain rates, and compare satellite-derived melt estimates with our in situ data.

Given the key role of calving for ice shelf mass loss, examining the driving factors for fracturing is an important step for  
65 predicting future ice shelf behaviour around Antarctica. Our analysis of the interactions between ice shelf melt, strain and complex ice shelf morphology at the NIS is therefore both important for assessing the future of this cold-cavity ice shelf, but also others that are subject to transverse fracturing.

~~to examine the cause of complex ice shelf morphology, its implications for ice provenance (e.g., meteoric vs. marine) and  
70 potential to fracture. The NIS is a cold-cavity ice shelf and has a thin suture zone where a transverse fracture formed around 1987, advected towards the ice shelf terminus while expanding laterally, and resulted in a large (213 km<sup>2</sup> in ice extent) calving event in 2016 (Dow et al., 2018). Around the time of this event, the ice surface strain patterns changed from extensional across-flow to extensional down flow within ~8 km of the ice shelf terminus and drove the formation of a new fracture over the thinnest region of the central NIS (Dow et al., 2018). This ice shelf is therefore an interesting site for examining how  
75 interactions between ice shelf morphology and strain in thin ice regions may enhance stress and cause fracturing.~~

~~We analyze and compare several datasets including ground-based and airborne ice penetrating radar (IPR), surface global  
80 positioning system (GPS) data, a satellite-derived digital elevation model (DEM), ice velocity-derived strain rate data, and oceanographic data. These data sets are used to examine the morphology of NIS and how this interacts with ice strain, basal melt and ice provenance, all important factors in shelf fracturing.~~

## 2. Site Description

The NIS, with an area of  $\sim 1800 \text{ km}^2$ , is located in Terra Nova Bay and is part of the Victoria Land Coast of the Western Ross Sea region in East Antarctica. The two primary glaciers that supply the NIS are the Reeves Glacier to the south and the Priestley Glacier to the north (Fig. 1a). The Priestley Glacier is up to  $\sim 900 \text{ m}$  thick near its grounding line (Morlighem et al., 2020) and has ice surface velocities up to  $\sim 180 \text{ m a}^{-1}$  (Gardner et al., 2020). The Reeves Glacier separates into two distinct branches as it flows around the Teall Nunatak and down a substantial ice fall at its grounding line. The Reeves Glacier is up to  $\sim 900 \text{ m}$  thick at its grounding line (Morlighem et al., 2020) with a surface ice velocity up to  $\sim 320 \text{ m a}^{-1}$  (Gardner et al., 2020). The grounding lines of the Priestley and Reeves glaciers have been estimated to be  $70 \text{ km}$  and  $40 \text{ km}$  from the ice shelf terminus, respectively (Mouginot et al., 2017).

The NIS ranges in thickness from  $900 \text{ m}$  at the Priestley Glacier grounding line to  $120 \text{ m}$  at the ice shelf terminus. The thinnest region is found in a  $30 \text{ km}$ -long surface depression (Fig. 2a), which runs east-west across the NIS along a suture zone where the floating ice from the Reeves and Priestley glacier branches converge (Alley et al., 2016; Bell et al., 2017; Baroni et al., 1991; Dow et al., 2018). A river was observed in the surface depression as early as 1974 and annually from 2014-2016 (Bell et al., 2017). During the melt seasons of 2014-2016 the river flowed into the transverse fracture prior to the calving event in April 2016 (Dow et al., 2018).

Inexpressible Island is a small land mass and pinning point located at the north-eastern end of the ice shelf terminus dividing the main NIS from the smaller Hell's Gate Ice Shelf. A polynya stretches from Hell's Gate Ice Shelf, along the terminus of NIS, and reaches the northern margin of the Drygalski Ice Tongue. This polynya plays an important role in sea ice production for the Ross Sea (Stevens et al., 2017) and is formed by katabatic winds, which also strips the NIS of much of its snow and firn cover leaving a significant portion of the surface as blue ice (Kurtz and Bromwich, 1983).

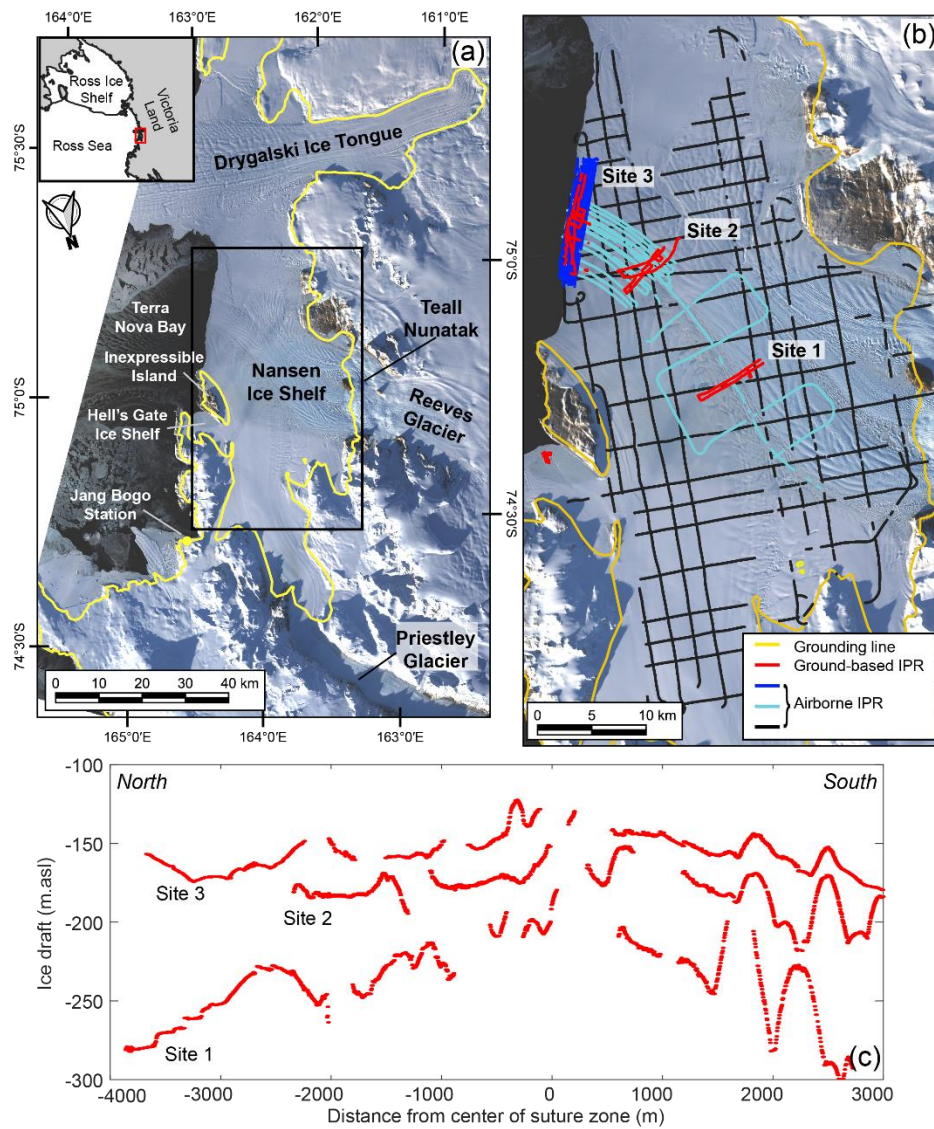


**Figure 1:** Site map with radar lines and cross sections. (a) The Nansen Ice Shelf (NIS) and grounding line/coastline (yellow line) from MEASUREs Antarctic Boundaries v2 (Mouginot et al., 2017) on a background image from Landsat-8 acquired March 22, 2017. Extent of (b) is shown by the black box. Inset: Victoria Land and western Ross Sea region, red box is the location of the NIS. (b) Ground-based ice-penetrating radar (IPR) lines at sites 1, 2 and 3 from November 2016 (red), Airborne IPR survey from January 2017 focused on the ice shelf terminus (dark blue) and suture zone (cyan), Airborne IPR survey from January 2017 of the entire NIS (black). (c) Three ice draft lines, one from each site. The location of these transects are shown in Fig. 2a.

### 3 Methods

#### 3.1 Ice penetrating radar

Between November 3-19 2016, ~80 km of ground-based ice penetrating radar (IPR) surveys were conducted on foot at three targeted sites focused on the suture zone of the NIS (Fig. 1b) resulting in a trace separation of ~1 m (see Appendix A), later down-sampled to a separation of 4 m. Some locations lacked a bed reflection, especially at Site 3 closest to the terminus, and repeat surveys verified that it was location specific. Ice surface elevation and precise location data were collected simultaneously with the radar data using a GPS receiver mounted on the IPR rig.

In addition to the concentrated ground-based radar surveys, a helicopter-based airborne geophysical survey was based out of the South Korean Jang Bogo Station between December 25 2016 and February 18 2017 (Lindzey et al., 2020; see Appendix A). In total, 1000 km of surveys were conducted over the NIS in both a grid-pattern and concentrated over the suture zone near the ice shelf terminus (Fig. 1 a, b). An error analysis was conducted using the cross-over surface elevations and ice thickness of both the ground-based and airborne radar and is detailed in Appendix A.

### 3.2 Ocean glider data

Between December 31, 2018 and January 10, 2019, a 1000 m depth rated G2 Slocum autonomous underwater glider was deployed along the NIS to collect observations of meltwater within the water column. Approximately 200 vertical profiles were completed across more than 100 km of transects back and forth along the ice shelf terminus, including ~10 km beneath the NIS, near the suture zone (Fig. 2 b,e). Hydrographic measurements were recorded on the glider using a SeaBird SBE-41 CTD (conductivity-temperature-depth) sensor to infer the presence of seawater modified by ice shelf melt. Other water column parameters were collected (e.g. dissolved oxygen, chlorophyll, turbidity, etc.) but will not be presented here.

Terra Nova Bay seawater is notably colder (potential temperature ~-2.0 to -1.5 °C) and more saline (practical salinity values ranging from ~34.70 to 34.85) in comparison to other Antarctic coastal waters. In the summer season, a layer of relatively warm and fresh Antarctic Surface Water develops in Terra Nova Bay that varies greatly in temperature (potential temperature > +1.0 °C) and salinity ( $S < 34.55$ ). Beneath this layer, the dense High Salinity Shelf Water (potential density  $> 1028 \text{ kg m}^{-3}$ ) is presumed to drive basal melt (Rusciano et al., 2013), resulting in the formation of Ice Shelf Water colder than the surface freezing point (potential temperature  $< -1.94^\circ\text{C}$ , Fig. 2d). We therefore take the presence of this cold water as evidence of ice shelf melt.

### 3.2.3 Digital Elevation Maps

Although the radar data provide information on the ice thickness and draft in our focused sites on the NIS, it is too sparse to accurately interpolate. As an alternative, for larger-scale morphological assessment of the ice shelf we use the 8 m resolution Reference Elevation Model of Antarctica (REMA) mosaic (Howat et al., 2019) for the NIS (Fig. 2a). We corrected the mosaic to the GLO04C geoid and applied hydrostatic calculations to invert for basal draft ( $B$ ) (Fig. 2b), using the equation:

$$B = S - \frac{S \cdot \rho_s}{(\rho_s - \rho_i)}, \quad (1)$$

Where  $S$  is the measured surface elevation above the GLO4C geoid,  $\rho_s$  is the density of sea water ( $1028 \text{ kg m}^{-3}$ ) and  $\rho_i$  is the density of meteoric glacial ice ( $917 \text{ kg m}^{-3}$ ). The zone of firm-free blue ice covers the regions of ground-based radar survey but firm is present towards the grounding line of Reeves Glacier and Inexpressible Island, and therefore in these regions the hydrostatic calculations are less accurate. We lack information on the thickness of firm in these regions precluding the inclusion of different density profiles in our application of Eq. 1. Assuming a REMA surface elevation error of  $< 1 \text{ m}$  (Howat et al., 2019), the hydrostatic thickness in the firm-free region has an associated error of  $\pm \sim 10 \text{ m}$ . We use this REMA-based thickness and basal draft product primarily for mapping purposes. We perform an analysis comparing radar ice thickness to hydrostatic thickness but, instead of the REMA product, we apply ~~We also apply~~ Eq. 1 to our in situ GPS ice surface elevation data to compare directly with the recorded radar ice thickness.

155



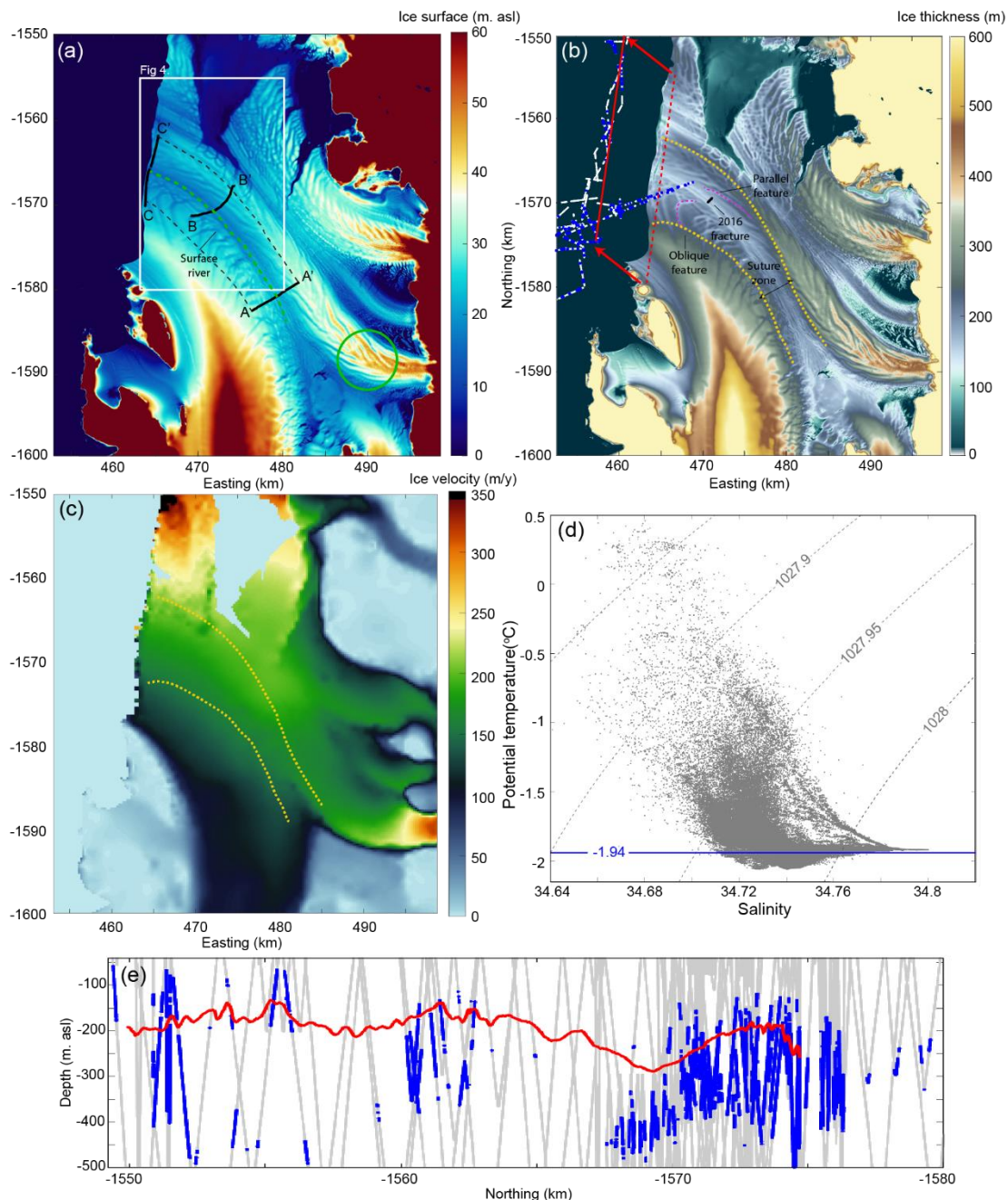


**Figure 2:** NIS DEMs (a) REMA ice surface elevation with the three transects in Fig. 1b and Fig. 3 plotted in black. The dashed black lines show the edge of the polygon calculated for flux gate analysis. The extent of Fig. 4 is shown by the white box. The green circle highlights an area referenced in the text in section 5.1. The DEM beyond the ice shelf terminus is set to 0 m due to the presence of data in the mosaic from prior to the 2016 calving event (b) Ice thickness DEM from hydrostatic calculations applied to (a) and assuming no firm. Blue points are the locations where Ice Shelf Water meltwater was detected by the ocean glider with white points indicating all other locations where glider data was collected between 40 and 500 m depth. The dashed red line shows the location of REMA hydrostatic ice draft plotted in (e), adjusted to the downstream location of the glider data (solid red line). (c) Annual ice surface velocity (2018) from ITS\_LIVE (Gardner et al., 2020) with the suture zone marked by the yellow dashed lines. (d) Temperature-salinity plot from the ocean glider data showing all data plotted in white and blue in (a). The -1.94 °C blue line shows the temperature below which water is assumed to be Ice sShelf meltwa Waterter. (e) Glider observations at intermediate depths (40-500 m). The locations of Ice sShelf meltwWater are shown in blue, whereas all other observations are in grey. The solid red line indicates ice shelf draft from REMA hydrostatic inversions, projected over the glider transect.

170 **3.3.4 Fluxgate analysis**

To assess the change in ice shelf shape in the suture zone as it advects downstream, we conducted a fluxgate polygon analysis following Neckel et al (2012) using cross-sections from radar and ice surface elevation transects, one from Site 1 (closest to the grounding line) and one from Site 3 (closest to the ice shelf terminus). We use streamline analysis applied to the beginning and end of the Site 1 cross-section with the 2018 ITS LIVE Landsat 8 derived annual velocity database (Gardner et al., 2020) to determine where the cross-sections intersect and we use these streamlines at a resolution of 50m to complete the polygon (Fig. 2a). For ice thickness along the streamlines we use the REMA hydrostatic product (section 3.2). The ITS LIVE dataset is then used to extract velocity vectors along all sides of the polygon.  
~~, along with velocities at these sites extracted from the 2018 ITS LIVE Landsat 8 derived annual velocity database (Gardner et al., 2020).~~

175  
 180 ~~These lines are separated by 22 km and, in cross-section, common basal features are identifiable as apexes (thinner ice regions) and keels (thicker ice region, deeper in the ocean). Using these basal features, we chose boundaries (shown in Fig. 3a and c by the dashed lines) and calculated the~~ The cumulative ice flux gain or loss ( $\Phi$ ) is calculated using the following equation:

$$\Phi = \sum_{i=2}^{i=N-1} v(i) \cos \alpha(i) H(i) di , \quad (2)$$

185 where  $i$  is the position along the edge of the polygon,  $N$  is the total number of positions in the fluxgate,  $v$  is the ice flow speed at polygon position  $i$ ,  $\alpha$  is the angle between the velocity vector and the direction perpendicular to the transect,  $H$  is the ice thickness, and  $di$  is the spacing between polygon positions. Error in the fluxgate calculation is determined by applying the radar thickness uncertainty discussed in Appendix A3. Volume gain or loss over the polygon is converted to mass loss assuming an ice density of  $917 \text{ kg m}^{-3}$ .

190

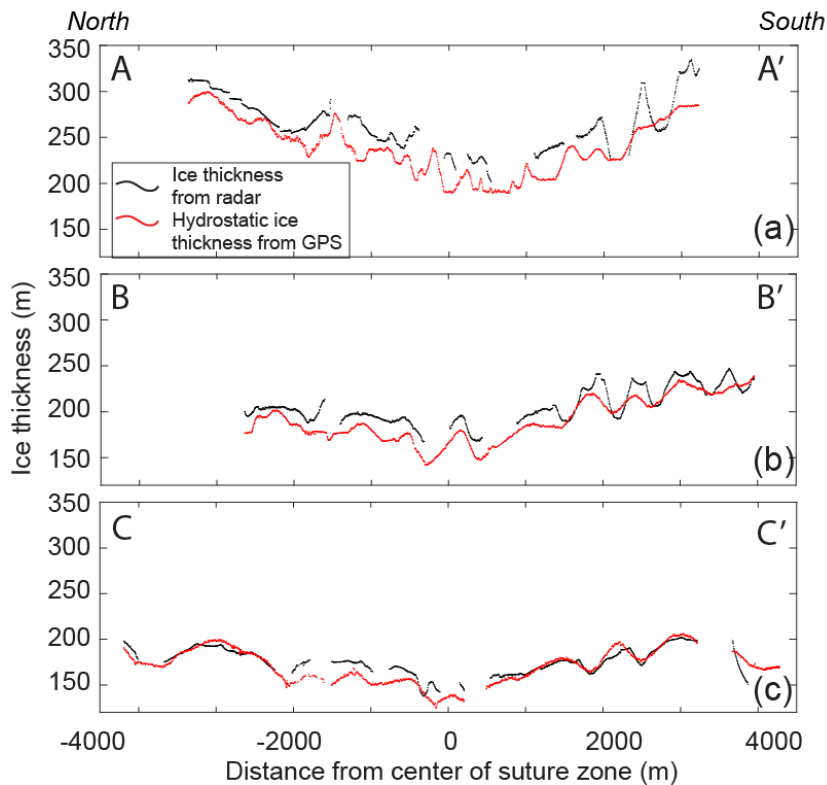


**Figure 3:** Cross-ice shelf transects of ice thickness from radar measurement (black) and from hydrostatic balance calculations using *in situ* GPS surface elevations (red) at (a) Site 1, (b) Site 2 and (c) Site 3 on the NIS. The ~~colored dots represent where the basal draft apexes and keels were compared between sites. The dashed grey lines show the limits of the flux gate calculations. Transects~~ are marked on Fig. 2a.

### 3.4.5 Strain rates

High resolution NIS ice surface velocity data were obtained from GoLIVE (Scambos et al., 2016). The closest nearly cloud-free period (September 29 – October 31, 2016) prior to the November 2016 IPR surveys was selected. GoLIVE velocities were used here instead of ITS\_LIVE velocities because the latter has an annual temporal coverage between image pairs, which obscured smaller-scale velocity features with short wavelengths. ~~The relationship between velocity vectors and vertical strain rate on an ice shelf is related by conservation of mass:~~

$$\dot{\epsilon}_{\perp} = \dot{\epsilon}_{xx} + \dot{\epsilon}_{yy} + \dot{\epsilon}_{zz} = 0, \quad (3)$$

~~where  $\dot{\epsilon}_{\perp}$  is the net strain rate of the ice, which is equal to zero and  $\dot{\epsilon}_{xx}$ ,  $\dot{\epsilon}_{yy}$  and  $\dot{\epsilon}_{zz}$ , are the strain rates parallel to principal x, y and, z axes respectively (Weertman, 1973).~~ We reoriented the GoLIVE velocity vectors so that the x direction is transverse and the y direction is longitudinal (down-flow) to the ice shelf flow direction. We then calculated the principal strain in the longitudinal and transverse directions using equations detailed in Dow et al. (2018) and Alley et al. (2018) with a length scale of 300 m, the pixel size of the GoLIVE velocity data (Fig. 4 b,c). Our approach of applying a length scale the same size as the pixel size follows the suggestions of Alley et al (2018) who state that such an approach is appropriate for ice shelves with highly variable basal draft topography. The consistency of transverse strain features at NIS across multiple years is shown in Fig 5. where we also plot the larger-scale regional shear, longitudinal and transverse strain rates.

~~We ran a sensitivity test with a length scale of 600 m, which produced similar results in both spatial pattern and magnitude of strain rates, but with smaller strain rate magnitudes in the suture zone on the order of  $-0.08 \text{ year}^{-1}$  or less. We interpolated the 2016 strain values from the 300 m length scale calculation to the radar data locations to assess the relationship between topography and ice surface strain on the NIS (Fig. 4).~~

### 3.5 Ocean glider data

~~Between December 31, 2018 and January 10, 2019, a 1000 m depth-rated G2 Slocum autonomous underwater glider was deployed along the NIS to collect observations of meltwater within the water column. Approximately 200 vertical profiles were completed across more than 100 km of transects back and forth along the ice shelf terminus, including  $\sim 10$  km beneath the NIS, near the suture zone. Hydrographic measurements were recorded on the glider using a SeaBird SBE 41 CTD (conductivity temperature depth) sensor to infer the presence of meltwater. Other water column parameters were collected (e.g. dissolved oxygen, chlorophyll, turbidity, etc.) but will not be presented here.~~

~~Terra Nova Bay seawater is notably colder (potential temperature  $\sim 2.0$  to  $1.5$  °C) and more saline (practical salinity values ranging from  $\sim 34.70$  to  $34.85$ ) in comparison to other Antarctic coastal waters. In the summer season, a layer of relatively warm and fresh Summer Surface Water develops in Terra Nova Bay that varies greatly in temperature (potential temperature  $> +1.0$  °C) and salinity ( $S < 34.55$ ). Beneath this layer, the dense High Salinity Shelf Water (potential density  $> 1028 \text{ kg m}^{-3}$ ) is presumed to drive basal melt (Rusciano et al., 2013), resulting in the formation of ice shelf meltwater below the *in situ* freezing point (potential temperature  $< -1.94$  °C), making the water supercooled (Fig. 2d). We therefore take the presence of this supercooled water as evidence of ice shelf melt.~~



#### 4.1 Nansen Ice Shelf morphology

Satellite products providing surface topography in the Antarctic are now high resolution (8 m horizontal from REMA mosaic) and provide excellent detail for analyses of surficial processes (Fig. 2). Using REMA hydrostatic thickness and our IPR data, the suture zone where the Priestley and Reeves glaciers first converge has an ice thickness of 200 m. The initial width of this thin-ice region is ~4.5 km with a difference in thickness of 50 m between the thin center and the thicker margin of the suture zone. Within 15 km of the terminus, the thin-ice region widens to 10 km with a draft difference of 90 m and 60 m, respectively, between the center of the suture zone and the northern and southern suture zone margins. At the terminus, the northern flank of the thin-ice region is wider (6 km) than the southern flank (4 km) with an average ice draft slope of ~1.3° and ~1.1° at the ice shelf terminus, respectively (Fig. 1c).

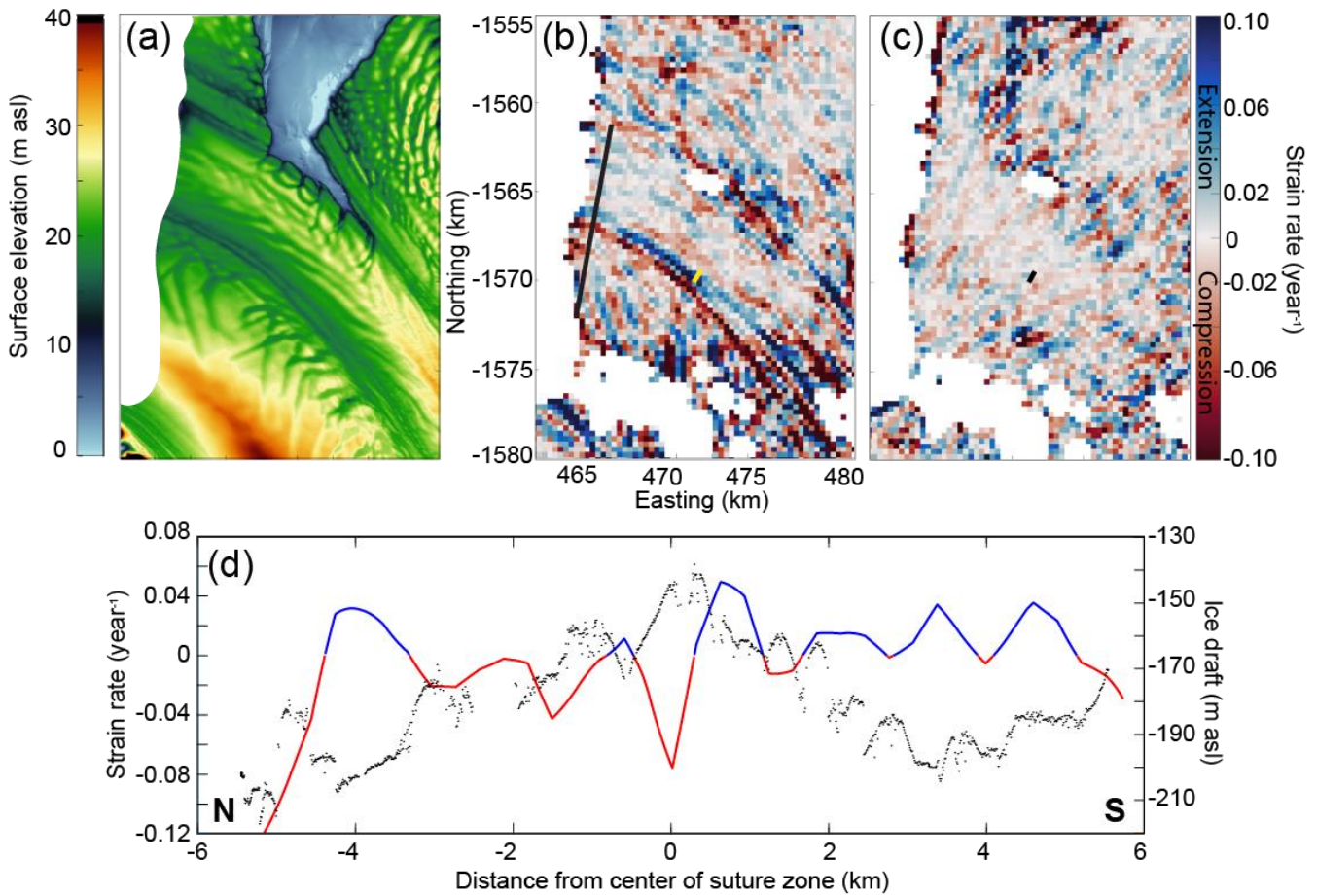
240

The combination of the larger-scale DEM and the smaller-scale IPR data indicate that there is a complex morphology consisting of multiple basal fractures, within the suture zone (Bell et al., 2017). These fractures originate upstream in the respective floating margins of Priestley and Reeves ice, prior to the convergence of the ice bodies. Within the suture zone, the fractures are discrete semi-continuous features that run parallel (on the southern side) or oblique (on the northern side) to the center of the suture zone (Fig. 2b). These basal features are altered as they advect downstream but we continue to refer to them as basal fractures for consistency (Fig. 2). The southern flank fractures are always parallel to the suture zone but are discontinuous and range from 15 – 25 m in height with a width of ~500 m on average (as determined from our radar data; see Fig. 3). On the northern flank, the fractures are also ~20 m high and ~500 m wide (Fig. 3) and are 3-5 km long near the ice shelf terminus (Fig. 2). In contrast to the southern fractures, these sweep away from the center of the suture zone to the north following a semi-circular pattern, and curve up to 90° from their original orientation.

250

There were several regions on the NIS where the ice-ocean boundary was not visible in the airborne and ground-based radar record (Fig. 6 a,d). Comparing these regions with the REMA hydrostatic thickness map shows they are associated with the thinnest region in the suture zone and with the basal fractures on both sides of the suture zone. Given the abundance of clear ice base signals in the remainder of the radar data, it is likely that these “echo-free zones” represent marine ice formation and/or frazil ice accumulation (Holland et al., 2009). The lack of radar echos in these regions are likely due to the presence of unconsolidated frazil ice at the base of meteoric ice (Fricker et al., 2001; Tison and Khazendar et al., 2001). On the ice surface, in the suture zone, there are many stripes of clear blue ice between larger regions of white aerated ice which also produce no radar echos (Fig. 6c). These can be traced back to the Reeves Glacier ice fall where crevasses fully fracture through the ice column, fill with sea water and refreeze (Khazendar et al., 2001). The filled crevasses are then advected and stretched, producing visible stripes parallel to the ice flow direction along the suture zone.

260



265

**Figure 4:** (a) NIS REMA mosaic surface elevation DEM. NIS ice surface (b) transverse and (c) longitudinal strain rate calculations from 2016 GoLIVE velocity data. The black line is the extent of the airborne radar transect shown in (c). The yellow/black line shows the location of the new 2016 fracture location. (d) Profile of the radar transect showing ice shelf draft (black) and strain rate (red: compression; blue: extension) interpolated along the transect. The extent of the region in Fig. 4b and c is shown in Fig. 2a.

270

#### 4.2 Strain rates

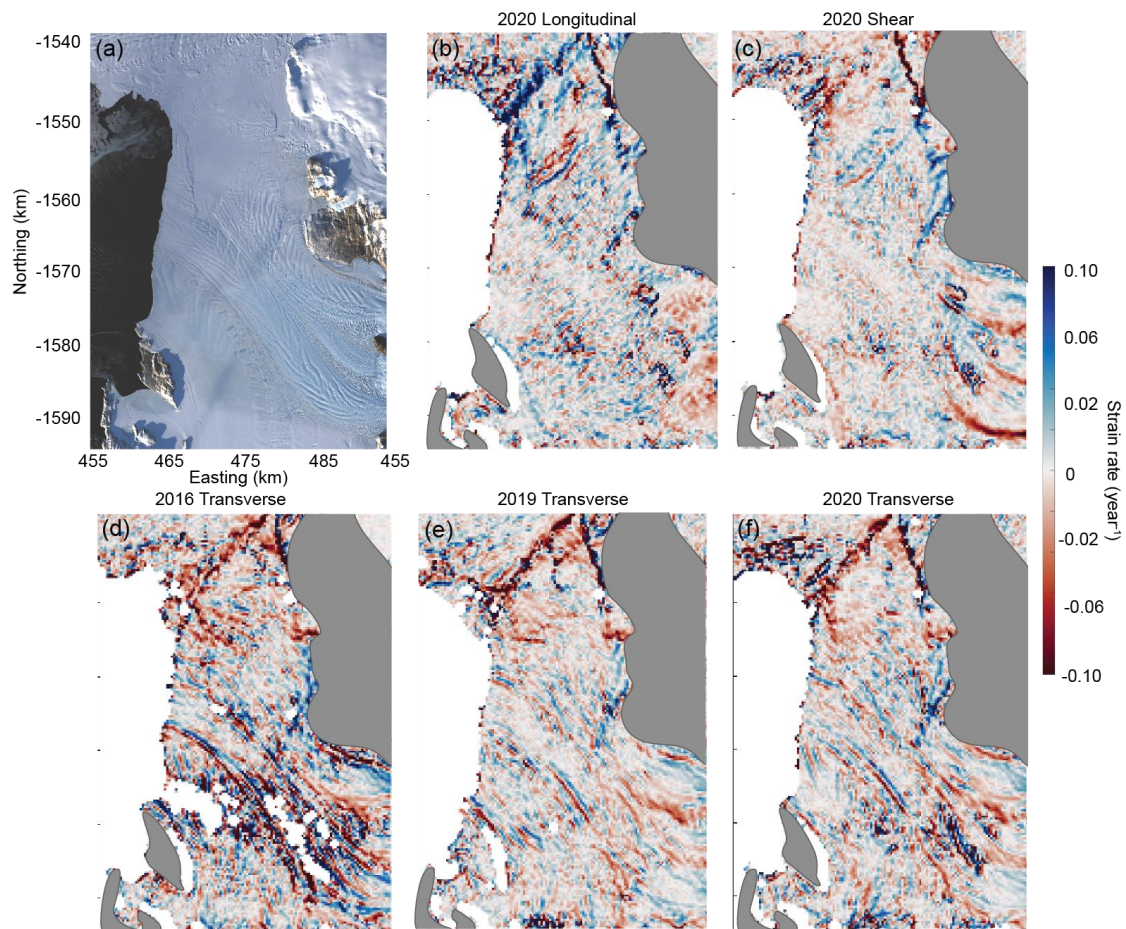
In order to determine whether the suture zone fractures complex basal morphology of the ice shelf impacts compressional and extensional strain we show horizontal transverse strain rates derived from 2016 GoLIVE ice surface velocity of the NIS (Fig. 4b) and a cross-section of strain rates plotted against the basal draft (Fig. 4d). We note that the patterns of strain presented here are also visible in NIS strain rate maps from multiple years, at different times of the year, and therefore appear to persist over time (Fig. 5).

275

Along the center of the suture zone there is an alternating region of horizontal compression (red) on the northern side and extension (blue) on the southern side: both regions have widths of ~800 m. When compared with the ice shelf draft, the switch between compression and extension occurs at the apex of the thin-ice suture zone region (Fig. 4d), although with a strain pixel size of 300 m there may be some error in the location of this transition. The new suture zone surface fracture which formed in 2016 is located within the strongly extensional side of the suture zone (Fig. 4 b). To the north, where the basal fractures curve, there is compression at the apexes of the fractures and extension at the keels. The patterns of strain can be seen in the 2D map (Fig. 4b) as well as in the cross-section with the radar-derived basal draft (Fig. 4d).

280

On the southern side of the suture zone, the relationship between basal fractures and strain is less clear with compression in the apex of the first fracture at 1500 m from the center and again at 2800 m from the center at the apex of another fracture. Otherwise, the strain is generally extensional. Similarly, in the 2D map, the strain patterns do not seem to align particularly well with the fractures on the Reeves side. We also show the map of longitudinal strain rate in Fig 4c. The pattern and signal in the longitudinal strain rate is poorly resolved compared to the transverse strain rate in Fig. 4b.



290 **Figure 5:** (a) The Nansen Ice Shelf (NIS) from Landsat-8 acquired March 22, 2017. (b) Longitudinal strain rate from  
 GoLIVE velocity data acquired between October 10 and November 11 2020. (c) Longitudinal strain rate from the same data  
 as (b). (d) Transverse strain rate from GoLIVE velocity data acquired between September 29 and October 31 2016. (e)  
 Transverse strain rate from GoLIVE velocity data acquired between October 8 and November 9 2019. (f) Transverse strain  
 rate from the same data as (b).

295

### 4.3 Ice shelf melt rates

We aim to determine where mass loss or gain is occurring at this cold-cavity ice shelf with particular focus on the suture zone. First, we performed a polygon fluxgate analysis between two transects of the suture zone to assess how much mass loss occurs as the ice flows towards Terra Nova Bay. ~~The fluxgate width is determined by the shape of the suture zone, where the margins of each transect are defined as the respective edges of the thinner ice region. This therefore takes horizontal flux divergence into account.~~ Total volume loss within the polygon is  $0.0523 \pm 0.0083 \text{ km}^3 \text{ a}^{-1}$ , or a mass loss of  $0.048 \pm 0.0076 \text{ Gt/year}$ . The discharge at Site 1 is  $0.226\text{-}262 \pm 0.004 \text{ km}^3 \text{ a}^{-1}$  and at Site 3 is  $0.222\text{-}210 \pm 0.005 \text{ km}^3 \text{ a}^{-1}$  demonstrating an average cross-sectional mass loss of  $481\text{-}2364 \text{ m}^2 \text{ a}^{-1}$  as the ice flows  $\sim 22 \text{ km}$  between these two sites. It takes an average of 123 years for the NIS to flow over this distance using velocities extracted from ITS\_LIVE.

300

305 We also estimate melt rate with the IPR data to examine ice draft thinning between Sites 1 and 3 using four clearly identifiable  
keels and apexes in the ice draft in both locations. From these points, the vertical ice thickness change is 94 m (keel, cyan point  
on Fig. 3a,c), -57 m (apex estimated due to the lack of radar return at the tip of the ridge; red point), 119 m (keel; blue point),  
and 85 m (apex; green point). This translates to average vertical melt rates of 0.75 m a<sup>-1</sup> (keel), 0.45 m a<sup>-1</sup> (apex), 0.95 m a<sup>-1</sup>  
310 the same section of ice, the change in shape may be due to differences in initial fracture formation. To estimate the cause of  
the mass loss between Site 1 and 3. We therefore also compare these values to examine ice shelf basal melt rates derived from  
Cryosat-2 satellite radar altimetry data provided as a grid with 500 m spatial resolution over the NIS (Fig. 5a7a; Adusumilli et  
al., 2020). The basal melt rates from Cryosat-2 indicate there are regions of freeze-on (shown by negative values) initiating  
where the suture zone begins with a maximum estimated mass gain of  $\sim 2 \pm 0.5 \text{ m a}^{-1}$  (Fig. 75a). At Site 1, the maximum mass  
315 gain is  $1.3 \text{ m a}^{-1} \pm 0.5 \text{ m a}^{-1}$ . Within the suture zone, there is then a transition into a region of melt 4 km upstream of Site 2. Site  
2 itself is close to the maximum melt rate in the suture zone of  $0.6 \text{ m a}^{-1} \pm 0.5 \text{ m a}^{-1}$ . The record does not cover Site 3 but the  
closest region has higher melt rates than Site 2 ( $\sim 1 \pm 0.6 \text{ m a}^{-1}$ ), although this may be unreliable due to the 2016 calving event,  
which is within the window of altimetry data amalgamation.

320 ~~It is possible that mass loss is due primarily to surface melt and sublimation, which was estimated by Bromwich and Kurtz  
(1984) to be 0.25 m a<sup>-1</sup> and by Bell et al. (2017) to be 0.5 m a<sup>-1</sup>. To investigate this, we integrate the basal shelf melt rates  
between Site 1 and Site 3 using the Cryosat 2 basal melt dataset along with ITS\_LIVE 2018 ice surface velocities and flow  
vectors (Fig. 5b). The basal melt map has data up to 2 km away from the Site 3 transect (Fig. 5a) and so cumulative basal melt  
will be slightly underestimated using this technique. Similarly, we calculate cumulative surface mass loss between the two  
325 sites using a uniform surface ablation rate of 0.25 m a<sup>-1</sup> and 0.5 m a<sup>-1</sup>. We compare these values of cumulative basal and surface  
ablation with the IPR derived thickness change between the sites. Because of the presence of basal features that are not fully  
aligned between the sites, we also provide a smoothed thickness change using a locally weighted least squares regression filter.  
The results demonstrate that, because of the initial freezing upstream in the middle of the suture zone, the central region has  
net zero change in basal melt. However, the steeper margins of the suture zone have sufficient basal melt to explain  $\sim 50\%$  of  
330 the thickness change. If this basal melt is combined with a uniform surface ablation of 0.5 m a<sup>-1</sup>, there is a good correspondence  
between the results, particularly at the northern margin of the suture zone where the cumulative mass loss estimates are within  
4 m of the smoothed measured mass loss. Towards the center of the suture zone there is a difference up to 24 m between the  
smoothed measured mass loss and the cumulative mass loss estimates. A lower surface ablation rate of 0.25 m a<sup>-1</sup> produces a  
lower total mass loss compared to the measured thickness change. Taking the 0.5 m a<sup>-1</sup> surface ablation rate, the remaining  
335 50% of thickness change at the margins and 100% of the thickness change in the suture zone center can be attributed to surface  
ablation processes (Fig. 5b). Some of the latter can be attributed to the ephemeral Nansen River, although this focuses frictional  
melt into two narrow (<100 m wide) channels in the middle of the suture zone to a maximum erosional depth of 2 m as  
determined from our IPR transects.~~

340 It is possible that mass loss is due primarily to surface melt and sublimation, which was calculated by Bromwich and Kurtz  
(1984) to be 0.25 m a<sup>-1</sup> and by Bell et al. (2017) to be 0.5 m a<sup>-1</sup>. To investigate this and where basal melt may be occurring at  
the ice-ocean interface, we extract streamlines between Site 1 and Site 3 and apply Lagrangian methods as described in Das et  
al (2020) to estimate strain thinning, basal melt and surface melt along those streamlines:

$$\Delta H = \int_{t_1}^{t_2} -w_b - w_s - H\nabla \cdot \mathbf{V} dt$$

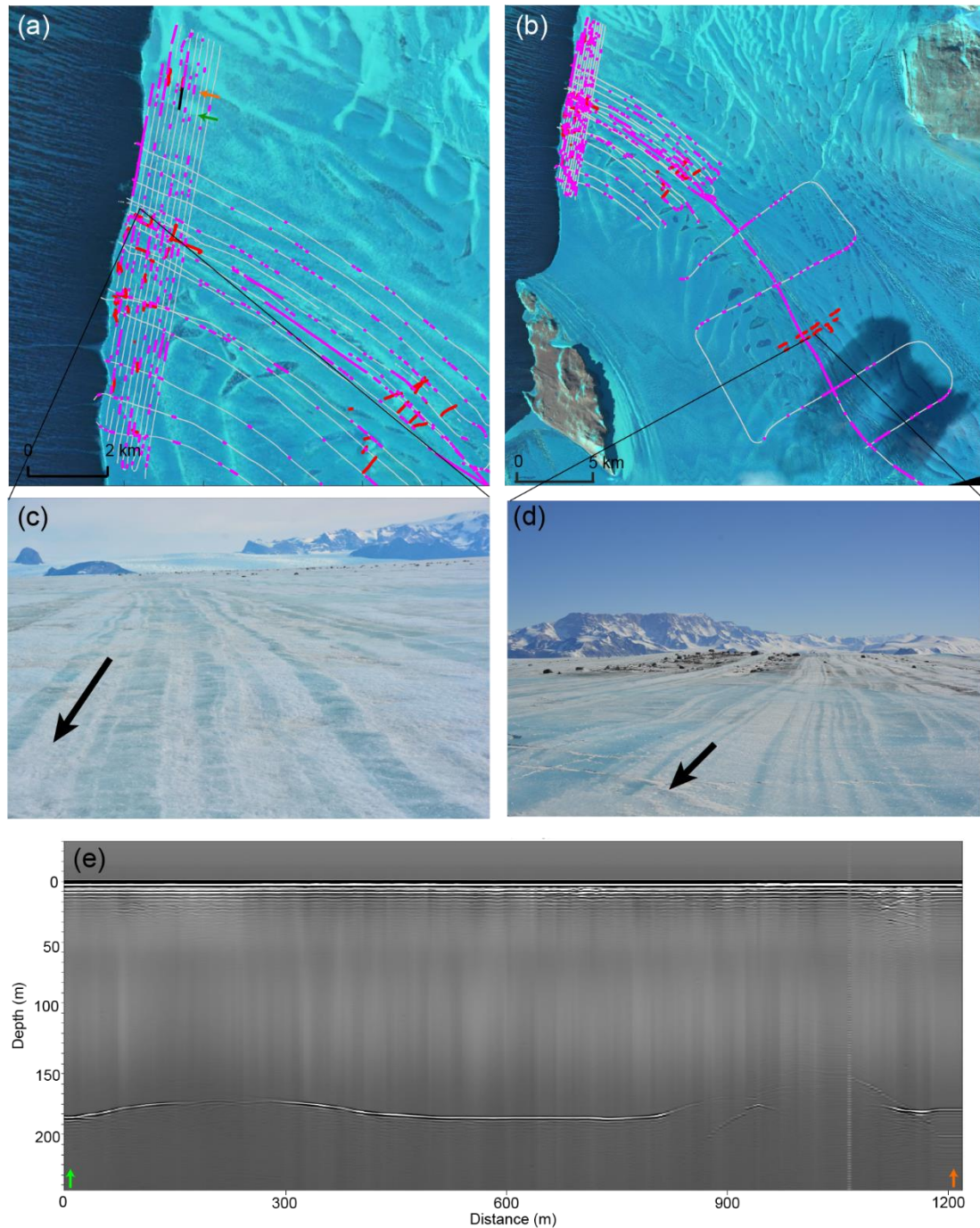


345 where  $w_b$  is basal melt,  $w_s$  is surface melt,  $\nabla \cdot \mathbf{V}$  is the ice velocity divergence from horizontal, and  $t_1$  and  $t_2$  are the times that  
ice passes through Site 1 and Site 3. Cumulative basal melt along the streamlines,  $w_b$ , is calculated from the Cryosat-2 basal  
350 melt dataset (Adusumilli et al., 2020). However, the basal melt map only has data up to 2 km away from the Site 3 transect  
(Fig. 7a) and so cumulative basal melt will be slightly underestimated using this technique. Similarly, we calculate cumulative  
surface mass loss,  $w_s$ , between the two sites using a uniform surface ablation rate of  $0.25 \text{ m a}^{-1}$  and  $0.5 \text{ m a}^{-1}$ . Because the  
355 region we are examining is composed of exposed blue ice we do not take accumulation into account. Velocity divergence for  
strain thickness change is calculated from ITS LIVE 2018 ice surface velocities and flow vectors (Gardner et al., 2020; Fig.  
7b). This analysis assumes steady state surface melt, basal melt, and ice velocity. The average time for ice to travel between  
Site 1 and Site 3 is 120 years, which means that some alteration of these rates may have taken place producing errors in our  
analysis, although with a cold cavity this is likely less of an issue than in regions of the West Antarctic for example (Das et al.  
2020). We compare the values of cumulative basal and surface ablation and strain thinning with the IPR-derived thickness  
360 change between the sites (Fig. 7b). Because of the presence of basal features that are not fully aligned between the sites, we  
first smooth the thickness at each of Site 1 and Site 3 using a locally weighted least squares regression filter before calculating  
the thickness change.

The average thickness change between Site 1 and Site 3 is 80 m (Fig 7b). The cumulative basal melting analysis suggests that,  
365 because of initial freezing upstream in the middle of the suture zone (see Fig. 7a), the central region of the suture zone has net  
zero change in basal melt. However, the steeper margins of the suture zone have sufficient basal melt to account for ~20 m of  
thinning at the ice base between Site 1 and Site 3. If we combine this thinning from basal melt with a uniform surface ablation  
rate of  $0.25 \text{ m a}^{-1}$  it produces ~50 m less thinning compared to the measured thickness change. However, when the thinning  
from basal melt is combined with a thinning due to a uniform surface ablation of  $0.5 \text{ m a}^{-1}$ , there is a good correspondence  
370 between the estimated cumulative thinning rate and the measured thinning, particularly at the northern margin of the suture  
zone. Thickness change due to strain thinning is limited to <13m between Site 1 and Site 3.

Finally, to determine whether the calculated basal melt in the suture zone is observable with *in situ* data, we plot the ocean  
glider data representing the location of Ice Shelf Water (ISW, identified by potential temperature <  $-1.94 \text{ }^\circ\text{C}$ ) cold, fresh, ice  
375 shelf meltwater on Figures 2b, and 5. This ice shelf meltwater ISW was distributed along the NIS terminus at intermediate  
depths, beneath the warm Summer Antarctic Surface Water and above the deep High Salinity Shelf Water. There are three  
regions where this water appears. The southernmost, adjacent to Drygalski Ice Tongue, had ISW meltwater at depths between  
58-490 m. The second region of ISW meltwater was towards the middle of the ice shelf with depths between 113-397 m. Our  
IPR data show that the draft of the NIS adjacent to this cold water meltwater mass ranges from 150-190 m in depth. The third  
region of ISW meltwater was close to Inexpressible Island at the northern margin of NIS and had depths between 128-502 m;  
here the NIS draft ranges between ~160 and ~230 m depth (as determined from REMA hydrostatic calculations). The second  
380 region of ISW ice shelf meltwater at shallower drafts therefore may be linked to active melt occurring in the suture zone as also  
suggested by our analysis of our IPR data and satellite-derived basal melt rates.





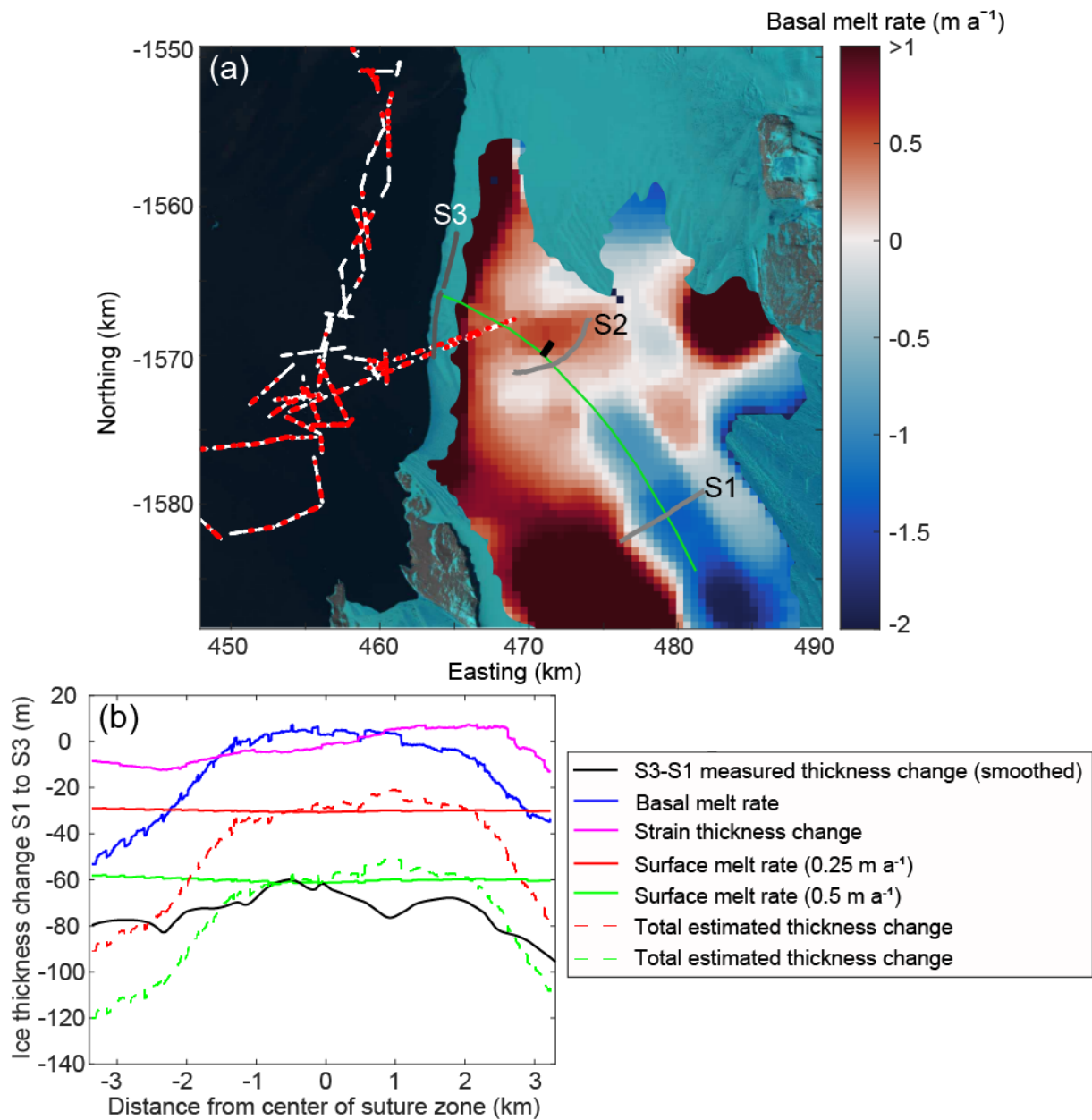
380 **Figure 6:** a) Sentinel image of NIS from October 5<sup>th</sup> 2016. Pink points are regions with radar signal dropout from the airborne  
radar and red points show signal dropout from the ground-based radar. The grey lines show the airborne radar tracks and the  
colored arrows and the black line show the extent of the radar transect shown in d). b) The same as a) but a larger-scale image.  
The dropout positions likely representing the presence of marine ice or frazil ice. The yellow line shows the 2016 fracture. The  
colored arrows and the black line show the extent of the radar transect shown in d). c) and d) photos of surface striping on  
385 NIS showing filled crevasses associated with the marine ice drop-out regions taken on November 11 and November 18, 2016,  
e) Radargram with a gain of  $t^{0.5}$  multiplied with the amplitude of each trace, where t represents time and signal  
dropout between traces 170-220 at a distance of 900-1100 m. The colored arrows correspond to those in a).

## 5 Discussion

### 390 5.1 Complex ice morphology

The ice draft elevation DEM we present computed using REMA surface elevation data reveals complex geometry of the suture zone. The thin ice of the suture zone is driven by a limited supply from the glaciers that only converge once they are already floating. The margins of the suture zone include regular basal fractures that have different characteristics depending on which side of the suture zone they form on, which appear to be driven by fracturing on the margins of the ice shelf before it converges  
395 in the suture zone. On the Reeves Glacier side, this fracturing can be seen in the ‘flame-like’ features near the ice fall (see green circle in Fig. 2a). These appear to be longitudinal crevasses that occur at the grounding line as the ice begins floating at the base of the ice fall and are re-oriented in the down-flow direction. The features are not continuous and perhaps represent periods of stick-slip motion on the ice fall causing periods of enhanced fracturing and flow followed by build-up of ice. These fractures can be traced downstream to the terminus in both REMA data (Fig. 2a) and in Landsat satellite imagery (Fig. 1a).

400 On the northern side, the equivalent features swing away from the suture zone by almost 90° as they approach the terminus. Again, tracing these upstream, they appear to originate from fractures on the southern margin of the Priestley Glacier. The fractures take on the sweeping shape likely due to the faster speed of Reeves Glacier (~200-250 m a<sup>-1</sup>) compared to Priestley (~150-200 m a<sup>-1</sup>), a behaviour that becomes increasingly enhanced towards the terminus (Fig. 2c). The difference in flow speed of the two portions of NIS is likely due to the pinning point of Inexpressible Island to the north (Fig. 4a). Examining the REMA  
405 elevation data for the upstream area of the NIS (as there are no *in situ* radar data in that location), the Priestley fractures first appear with lengths of 2 km. The floating Priestley Glacier ice thins and stretches as it advects downstream towards the terminus, causing these fractures to expand laterally northwards, with lengths up to 7 km. The basal fractures on the Priestley side result in hydrostatic depressions on the surface that are easily identifiable through water ponding on the surface during the brief (<25 days per year; Bell et al., 2017) melt season of this ice shelf (Fig. 6a).



410

415

**Figure 57:** (a) NIS basal melt rates averaged between 2010-2018 from Cryosat-2 data; data from Adusumilli et al. (2020). The 2016 surface fracture is plotted in black, and the site transects shown in Fig. 3 are plotted in grey. Red points are the locations where ice shelf Shelf meltwater Water was detected by the ocean glider instruments with white points indicating all locations where glider data was collected between 40 and 500 m depth. The center of the suture zone is shown in green. The background is a Landsat-8 image acquired on January 2, 2019. (b) Cumulative ice thickness change-mass loss between Site 1 and Site 3 calculated from IPR thickness change (black), Cryosat-2 basal melt data (blue), and two surface melt rates (red and green dashed lines), and strain thinning (pink). Total mass loss thinning (Cryosat-2 basal melt plus surface melt plus strain thinning) is shown by the solid cyan and red dashed red and green lines for surface ablation rates of 0.25 and 0.5 m a<sup>-1</sup>, respectively.

420

## 5.2 Hydrostatic equilibrium

Although the general features of basal fractures can be examined using REMA, ice shelf draft estimations that are extrapolated using hydrostatic balance calculations do not take bridging stress (i.e., flexural stress between areas of relatively thick ice) or

pinning points into account and therefore may not fully represent the ice thickness and basal ice morphology (Drews et al., 2015; Gladish et al., 2012; Mankoff et al., 2012; Vaughan et al., 2012). Our *in situ* ground-based and airborne radar thickness data provide high-resolution data of ice shelf draft features and can be compared with hydrostatically-derived thickness using simultaneously collected ~~surface elevation~~GPS data to test this at the NIS.

In comparing ice thickness data from the IPR cross-sections with thickness derived from GPS surface elevation and hydrostatic calculations we found that the best match is at Site 3 nearest to the terminus. At Site 1 and 2, further upstream, there was a vertical offset where the ice thickness measured using the radar was greater, on average, than the ice thickness derived from surface elevation measurements (Fig. 3). ~~This offset can be corrected by raising the surface elevation by an additional 2.5m and, given that we have not corrected for Mean Dynamic Topography (Griggs and Bamber, 2009) or tidal variation, some of this offset may be explained by these factors. Regardless of the mean thickness offset, the spatial pattern of hydrostatic thickness at Site 1 and 2 also does not accurately reflect the variable topography in this region.~~ For example, at Site 1 on the northern side of the suture zone, the basal fractures represented in the radar data are around 1600 m wide and 50 m high, which is similar to the fractures measured from hydrostatic balance (which are 1655 m wide and 53 m high). On the southern side of the suture zone, the radar thickness reveals fractures that are 448 and 522 m wide with heights of 64 m and at least 82 m. Yet in the thickness data derived from hydrostatic calculations, these fractures are difficult to discern and are limited in height (only up to 10 m). At Site 2, basal fractures on the southern side can be seen in the hydrostatic thickness profiles but are not fully defined; for example, a fracture measuring 49 m from apex to keel (~~blue to green dot, Fig. 3b~~) is visible in the hydrostatic thickness transect but at a height of only 20 m (Fig. 3b). However, at Site 3, near the ice shelf terminus, the fractures on both the northern and southern sides of the central suture zone are well represented in both the radar and the calculated hydrostatic thickness data. There, the southern fractures are 660 and 665 m wide with heights of around 26 m.

Our *in situ* data calculations demonstrate that the mismatch between hydrostatic ~~thickness-topographic features~~ and radar ~~ice thickness-topographic features~~ is therefore greater closer to the grounding line. This ~~could potentially be~~ likely due to bridging stresses ~~from the highly variable basal draft and/or from pinning of the ice shelf from valley walls or nunataks. However, the nearest pinning point is Inexpressible Island, 10 km to the north of Site 1. Given this distance, it is more likely that bridging stresses are~~ impacting the narrower basal draft features in the suture zone of the ice shelf (McGrath et al., 2012, Bassis and Ma, 2015), although this would have to be confirmed using modeling approaches. ~~However, o~~Our data suggest that bridging stresses are likely to obscure basal morphology only when the basal fracture features are narrow and tall; in this case narrower than ~500 m and taller than 60 m. This effect has been noted at other ice shelves (e.g., Raymond and Gudmundsson, 2005; Nicholls et al., 2016) although it was assumed that the features had to be significantly smaller than the ice thickness to remove the hydrostatic signature from the ice surface. Yet at Site 1 where we have the most significant difference between measured and estimated morphology, the ice thickness ranges between 200-330 m, ~ half of the width of the basal fracture features. Other factors such as the height of the features must also therefore play a key role in limiting hydrostatic surface signatures.

Our results suggest that, when using a larger-scale surface elevation dataset such as REMA to estimate ice thickness (as shown in Fig. 2b), although general characteristics of the ice shelf can be determined, basal morphology analysis would have similar limitations that we identified with our *in situ* GPS surface elevation data. Limited ability to detect complex ice draft geometry will inhibit applicability of ocean circulation models with km-scale resolution for ice shelves in the Antarctic (Nicholls et al., 2016).

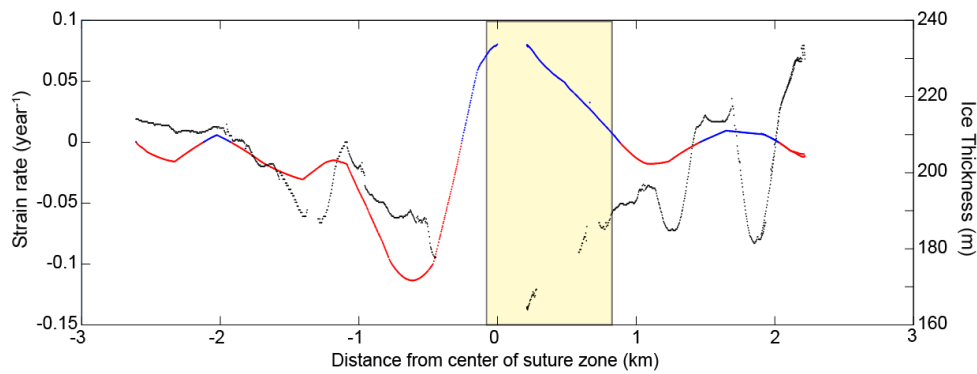


**Figure 8:** Site 2 transect ice thickness (black) with strain rate (red: compression; blue: extension) interpolated along the transect. The location of the new surface fracture formed in 2016 is blocked in yellow and intersected this IPR transect. Note the radar drop out in the region of fracture formation.

465

### 5.3 Ice shelf fractures and strain rates

There is a clear relationship between the northern flank basal fractures and the ice surface transverse strain rates (Fig. 4b, d) where extension occurs over the keels and compression over the apexes. This is likely driven by the hydrostatic balance forcing surficial bending to conform to the basal variation in ice draft, with deeper keels and shallower apexes driving the formation of hills and troughs on the ice surface, respectively. As described in Vaughan et al. (2012), who applied a thin bending beam and finite element model to examine the stresses caused by variable ice shelf draft, there will be compression in the thinner ice regions and extension over the thicker ice regions.

This pattern of variable strain is stronger on the northern side potentially due to the orientation of the basal fractures relative to the flow direction of the ice (~ up to 90°) in comparison with the southern basal fractures, which are parallel to ice flow. Drews et al. (2015) examined the Roi Baudouin Ice Shelf, and suggested that surface velocities and related strain rates from satellite observation may be sufficient to characterize basal channel morphology. This seems to also be applicable to the NIS basal features and may be a useful tool when examining areas with significant variability in basal draft that might not be visible in the hydrostatic balance calculations due to bridging stresses.

The stripe of compressive strain along the suture zone center adjacent to a stripe of extensional strain on the southern side is an interesting characteristic corresponding with the thinnest region of ice. The compressive strain on the northern side is likely due to the slower speed of Priestley Glacier coupled with pinning of this ice between Inexpressible Island and the Reeves Glacier ice. On the southern side, the extensional transverse strain is due to the faster speed of the less-constrained Reeves ice compared to Priestley's. Beyond the thinnest region of the suture zone there is more extension on the southern side of the ice shelf compared to the northern side (Fig. 4d). This spatial difference in strain may contribute to the more significant lateral stretching and dampening in draft of the southern basal fractures between Site 1 and Site 3 as shown in Fig. 1c.

The more significant extensional strain on the southern side explains why the 2016 fracture originates at the center of the suture zone and expands to the south, but does not extend into the compressive region to the north (Fig 4b). In 2016, the extent of this fracture reached as far as a compressive region associated with a basal fracture on the ~~northern~~southern side where the ice becomes thicker (Fig. 8). It should be noted that only the transverse strain rate map provides information on the compression and extension in the keels and apexes of the basal fractures, along with the extensional and compressional striping along the suture zone. If only longitudinal strain had been calculated, these features would have been missed. The transverse strain rate therefore appears to be the primary control on the patterned variability in extension and compression on the NIS and, although

490



larger-scale longitudinal extension played a primary role [as to](#) when the 2016 fracture formed (Dow et al., 2018), the transverse strain [and ice thickness](#) limited the lateral extent of the fracture.

#### 5.4 Marine ice

Evidence of fracture propagation rates across other Antarctic ice shelves, such as Larsen C, suggests that the presence of marine ice, particularly in suture zones, hinders fracture expansion due to its higher fracture toughness (e.g., Hulbe et al., 2010; McGrath et al., 2014; Borstad et al., 2017). Echo-free zones in the radar records in the thinner regions of NIS (Fig. 6d) suggest the presence of accreted marine ice and/or unconsolidated frazil ice; for the purposes of this discussion we will refer to both types as “marine ice” (Holland et al., 2009). Marine ice is known to inhibit radar returns from the ice-ocean interface as it absorbs the radar signal very effectively (Moore et al., 1994). With IPR data alone we cannot assess whether these losses of signal represent full thickness rifts with frozen seawater or as a result of frazil ice accumulation within regions of reduced ice draft. However, with the REMA hydrostatic DEM and our *in situ* survey of the ice shelf, it appears that the marine ice in the center of the suture zone originates from full-thickness fractures that refreeze with intruded ocean water at the base of Reeves Ice Fall. This is consistent with ice core analysis of marine ice frozen into a rift 7.5 km downstream of the Reeves grounding line by Khazendar et al. (2001).

Full rifts containing marine ice should therefore inhibit fracture propagation regardless of whether the fracture initiates at the surface or the base of the ice. However, it was across one of the regions of ‘striped’ ice with multiple full-thickness marine ice bands, and radar data echo-free zones, that the 2016 fracture formed (Fig 6a, [Fig. 8](#)). It is possible that the bands of marine ice are too thin to impede propagation of the fracture, although this would be interesting to test this hypothesis with fracture mechanics modelings. The fracture expanded southwards until it reached an area of meteoric ice, where, as mentioned above, transverse compressive strains dominate due to the basal morphology, preventing further expansion of the fracture. Borstad et al. (2017) suggested that the presence of a basal crevasse perpendicular to the fracture may hinder propagation of the fracture tip, and this may be another reason for the limited southern extension of the 2016 NIS fracture.

Outside of the central suture zone, regions of radar signal loss are associated with basal fractures and therefore likely due to the accumulation of marine or frazil ice within the fractures. Comparing the regions of marine/frazil ice accumulation in Fig 6a with the basal melt map in Fig. [5a7a](#), the transition between larger-scale basal freezing, located closer to the grounding line, to basal melting does not seem to impact the extent or number of echo-free zones associated with basal fractures. Marine or frazil ice is therefore present in at least the apexes of some of the basal fractures even towards the ice shelf terminus where melt rates increase to  $>1 \text{ m a}^{-1}$ . Given our analysis that most basal melt occurs on the steeper margins of the suture zone, this suggests that the basal fractures penetrated sufficiently far into the ice and filled with frozen ocean water (e.g., McGrath et al., 2014) such that some of the marine/frazil ice remains within these fractures in spite of the melting [on slopes at the base of rates calculated for](#) the NIS. Alternatively, ocean melt may be focussed on the deeper keels with frazil ice formation possible at the apexes of the basal fractures. The dampening of the amplitude of the basal features [as they advect](#) as shown in Figure 3, suggests that such differential melting and freezing may be occurring [\(see e.g. Khazendar and Jenkins \(2003\), Jordan et al. \(2014\), and McGrath et al. \(2014\)\).](#)

A full characterization of marine ice on the NIS would require a geophysical investigation with active seismic lines or *in situ* sampling and could elucidate useful information about cavity circulation under this ice shelf and establish whether the presence of the Terra Nova Bay polynya has an impact on basal ice accumulation. It would also allow ground truthing of the satellite melt map product.

In addition to examining regions of the NIS where mass may be accumulating in the form of marine/frazil ice, we are interested in where mass is lost. We also assess whether we are able to classify the thin ice suture zone of the NIS at the convergence of the Priestley and Reeves glaciers as a channel or whether it is a purely ice-dynamic feature with minimal oceanic enhanced melting. Even in a cold cavity, some enhanced melt would be expected with channelized flow and, as increasing numbers of ice shelf channels are being identified (Alley et al., 2016), including many in suture zones, it is important to establish the role they play in alteration of the ice shelf. Alley et al. (2019), who examined shear margins around the Antarctic, used the presence of polynyas to detect where the thinner ice of a suture zone has allowed enhanced oceanic flow and therefore can be classified as a channel. The NIS is associated with the substantial Terra Nova Bay polynya, a major sea ice producer in the region (Ciappa et al., 2012), which stretches the full width of the NIS. However, this is driven primarily by katabatic winds flowing over the ice shelf (Kurtz and Bromwich, 1983) and therefore we cannot use it for channelized flow classification. At the NIS, the difference in ice thickness between the suture area (~200 m thick) and the body of the ice shelf where the floating ice initially converges (~550 m on the Priestley side, ~300 m on the Reeves side) could drive ocean current acceleration and enhanced melt (Little et al., 2009). Furthermore, the change in shape of the suture zone as it advects downstream does suggest some alteration from ocean-driven melting. The thin-ice region has a longer, lower-gradient edge on the Priestley (northern) side and a steeper but shorter wall on the Reeves (southern) side, which may be due to Coriolis-forced enhanced melt towards the northern side of the channel. Coriolis-forced acceleration of currents along the flanks of channels causing enhanced melt has been identified in other basal channels around the Antarctic (Alley et al., 2016; Dutrieux et al., 2013; Gladish et al., 2012; Mankoff et al., 2012). The pinning of the Priestley ice between Inexpressible Island and the Reeves ice inhibits enhanced lateral stretching in this region, whereas the Reeves ice flows beyond lateral pinning points sooner and is therefore able to expand to the south. If driven by ice dynamics alone, it would be expected that the Reeves side of the suture zone would be the less steep flank as opposed to the Priestley. As the opposite occurs it suggests that the shape of the suture zone is altered by Coriolis-driven enhanced melt, with accelerated flow in the regions of highest basal draft driven towards the northern side of the suture zone.

We have also presented ~~several multiple~~ analyses of ice shelf melt including a flux gate calculation; ~~point analysis on the basal fracture apexes and keels (Fig. 3); IPR thickness change estimates between transects,~~ and cumulative melt rates on the surface and base between our IPR sites, derived from ice surface velocity data combined with satellite-derived basal melt rates (Adusumilli et al., 2020) and surface ablation ~~calculations estimates (Bromwich and Kurtz, 1984; Bell et al., 2017); Fig. 5a7a).~~ Each of these techniques has limitations. The flux gate ~~and cumulative melt~~ analysis, while taking account of horizontal strain, does not ~~allow for take into account potential~~ changing ocean ~~or surface~~ conditions over the >100 years for ice to advect the 22 km between Site 1 and Site 3. ~~The point analysis is applied to basal features related to crevasses, and the initial fracturing process may have caused different size and shapes of the keels and apexes. Finally, In addition,~~ the satellite-derived basal melt rates signals are close to the noise floor (uncertainty) of the dataset for the NIS. However, all ~~three methods of our results from both in situ and satellite-derived data~~ suggest that there is enhanced basal melt on the steeper slopes at the margin of the suture zone, ~~which gives us confidence in our results.~~ The central region of the suture zone, in contrast, appears to be dominated upstream by basal freezing, which is offset by melting closer to the terminus. Change in thickness in the thinnest central region is therefore primarily as a result of surface ablation (Fig. ~~5b7b).~~

The maximum melt rate in the suture zone from the basal melt map is  $\sim 0.6 \pm 0.5 \text{ m a}^{-1}$ , except for at the ice shelf terminus where rates increase to  $\sim 1 \pm 0.6 \text{ m a}^{-1}$ . Similarly, generally low melt rates ( $0.08\text{-}0.09 \text{ m a}^{-1}$ ) are predicted for the base of the nearby, cold cavity Ross Ice Shelf, with melt increasing to ~~4m-2 m~~  $\text{m a}^{-1}$  near its terminus (Stevens et al., 2020; Das et al., 2020). However, these rates are low compared to other ice shelves such as Getz Ice Shelf which has an area averaged melt rate of

4.15 m a<sup>-1</sup> (Wei et al., 2020), and ice shelves that come into contact with relatively warm circumpolar deep water have even higher basal melt rates, such as Pine Island Glacier ice shelf (30 m a<sup>-1</sup>; Dutrieux et al., 2013). Oceanographic data in Terra Nova Bay collected by Manzella et al. (1999) and by the ocean glider indicated relatively cold ocean water conditions, explaining why ~~basal/vertical~~ melt rates within the suture zone are likely to be small in comparison to the Amundsen Sea sector. 580 The basal ice loss rates over the steeper slopes at the edge of the suture zone (Fig. 4b) do, however, suggest an active melt component and that the suture zone is acting to channel water.

Comparing the satellite-derived basal melt rates (Adusumilli et al., 2020) with ~~the-our~~ ocean glider data, there is a good correspondence between the locations of ~~ISW/meltwater~~ near Inexpressible Island and the center of the NIS terminus, and the areas of enhanced melt from the ice shelf ~~suggested by the satellite data~~ (Fig. 5a7a). The ~~mISW/meltwater~~ pulse adjacent to 585 Inexpressible Island may originate from Priestley Glacier grounding line where subglacial drainage might impact the circulation and melt rates, although given the distance between the grounding line and the observed ~~freshwater-cold water~~ pulse (50 km), this warrants further investigation. Some of the ~~ISW/meltwater~~ observed by the glider underneath and directly offshore of the middle of the NIS terminus is at a depth that could be linked to the thinner draft of the NIS in the suture zone (150-190 m), where enhanced melt is observed both from our IPR analysis and the satellite derived basal melt rates. However, 590 it is more challenging to determine exactly where the deeper ~~ISW/meltwater~~ recorded by the glider originated from (Fig. 2c). In addition, the presence of sub-mesoscale eddies in the region near the NIS terminus may be impacting both the depth and location of the ~~ISW/meltwater~~ (Friedrichs ~~et al.~~, ~~in-review2022~~).

The transverse fracture discovered in 2016 occurs at the transition into the highest melt region of the suture zone (Fig. 5a7a). The formation of this fracture was argued to be due to an alteration of the strain regime from transverse to longitudinal 595 extension between 2014 and 2015, linked closely to the expansion and the calving of a fracture located much closer to the ice shelf terminus (Dow et al., 2018). However, as this strain transition occurred in the same region as the maximum melt, this region may be associated with a reduction in buttressing on the ice shelf cavity walls due to thinning ice, compared to further upstream. This suggests that with ocean warming and related melt, which will also alter the draft morphology and therefore the shelf strain rates, fracturing may occur further upstream and may laterally propagate more rapidly, allowing more frequent 600 calving events. To assess this would, however, require an ocean model driven with the complex morphology that we have identified in order to determine the relative roles of supercooling and melt in the ocean cavity and how this might change over time (Goldberg et al., 2019).

## 6 Conclusions

605 The Nansen Ice Shelf is a small, cold-cavity ice shelf, yet includes a variety of complex features due to the combination of ice dynamics, the shape of the embayment and interaction with the ocean. The primary causes of the complex morphology at Nansen Ice Shelf are the dynamics of upstream ice with basal fractures formed at the grounding line of Reeves Glacier and the floating margin of Priestley Glacier ice before they join together in a suture zone. Comparison between ground-based radar thickness data and ice surface GPS elevation hydrostatic calculations suggests that bridging stresses can significantly dampen 610 the vertical surface expression of the basal morphology, in this case particularly for basal features narrower than ~500 m and taller than 60 m. This is despite an ice thickness of between 200-330 m in this region suggesting that even features larger than the ice thickness may not be observable in satellite data.

Changes in the basal fractures as they advect downstream is evident in both the ice shelf draft and the strain rate maps, and 615 demonstrates the competing elements of horizontal variability in transverse strain and differential ice velocities on either side of the suture zone of these two glaciers. Application of only longitudinal strain rates would miss this complex relationship

between the basal fractures and the ice strain. Although longitudinal strain can provide information about controls initiating a transverse surface fracture that was identified in the field in 2016, the more complex system demonstrated by the transverse strain rates, which appears to limit the lateral extent of the fracture, suggests that for analyses of ice shelf stability, multi-directional strain rates must be taken into account.

The basal fracturing leads to accumulation of marine ice in the full-thickness rifts associated with Reeves Glacier and marine/frazil ice in the tips of basal fractures associated with Priestley Glacier, as demonstrated by radar echo-free zones and stripes of blue ice on the ice shelf surface. The 2016 transverse surface fracture formed in the center of the suture zone in a region of full-thickness rifts now filled with marine ice, which has previously been suggested to limit fracture propagation due to higher fracture toughness. The limited width of the re-frozen rifts (often less than 5 m) may restrict the ability of the marine ice to hinder fracture propagation.

Our analysis of changes in ice morphology, flux gate volume, oceanographic data indicating the presence of meltwater, Ice Shelf Water, and satellite-derived ice shelf basal melt suggest that active oceanographic melt is occurring within the suture zone. Basal melt is greatest on the steep margins of the suture zone whereas surface ablation dominates mass change in the thinnest central region. *In situ* sampling is required to determine the location and rates of melt, for example whether it is focussed only on the keels between basal fractures. The Nansen Ice Shelf basal melt rates are small compared to warm cavities in the Amundsen Sea region. However, it may have played a role in active fracture in a higher melt region within the suture zone of the Nansen Ice Shelf. ~~In 2016 a new transverse fracture was discovered in this region, and a rift that originally formed in this location caused a large calving event.~~ The combination of ice morphology, channelized melt, and strain patterns within the ice shelf all appear to play a role in the formation of fractures in this ice shelf, which result in large-scale, periodic calving events (Dow et al., 2018). These findings warrant investigation of other ice shelves with transverse fractures to establish causal mechanism behind fracturing at those locations and whether they are likely to lead to large-scale calving events.

## 640 Appendix A: Ice Penetrating Radar methods

### A.1 Ground-based radar

An IceRadar (Blue Systems Integration Ltd.) equipped with 10 MHz resistively-loaded dipole antennae separated by 15 m was used to collect the on-foot radar lines (Mingo and Flowers 2010). The IPR transmitter pulsed 512 times per second and the average of a stack of 50-256 traces were recorded by the receiver at an interval of 1-3 seconds.

Precise location data were simultaneously collected at 1 Hz using a Topcon Hiper V L1/L2 Global Navigation Satellite System (GNSS) receiver placed next to the IPR receiver. GNSS data were subsequently processed using Natural Resources Canada's (NRCan) precise point positioning (PPP) service and corrected to the GL04C geoid datum (e.g. Griggs and Bamber, 2011), after subtracting the height of the GNSS antenna center above the ice surface (Greene, 2021). Radar Tools (modified from release 0.4; github ID: njwilson23/irlib) was used pick the air wave and reflected wave from each trace. Ice thickness ( $H$ ) was calculated as:

$$H = \sqrt{\frac{vv^2(t+d/c)^2}{4} - \left(\frac{d}{2}\right)^2}, \quad (\text{A1})$$

where  $d$  is the antenna separation distance (15 m),  $t$  is the two-way travel time (s) from the air wave to the reflected wave,  $c$  is the speed of the radar wave in air ( $3 \times 10^8$  m s<sup>-1</sup>) and  $v$  is the speed of the radar wave in ice ( $1.68 \times 10^8$  m s<sup>-1</sup>; Fujita et al., 2000).

## A.2 Airborne radar

A radar system was installed on an Aérospatiale AS-350 helicopter in a fixed boom, and was complemented by a laser altimeter, camera, Global Positioning System (GPS), and an internal navigation system (INS) for precise positioning. Two of the three fixed booms attached to the bottom of the helicopter contained separate antennae, installed in a cross-track polarized dipole arrangement, that both transmitted and received independently, with 60 MHz center frequencies, 15 MHz chirp bandwidths, and 1  $\mu$ s pulse width.

## A.3 Error analysis

Where survey lines crossed, ice thickness and surface elevation values were compared at points of closest approach (within a maximum distance of 20 m) to evaluate repeatability and bias between datasets. Ground-based IPR ice thickness ‘crossover’ points (n= 13) agreed to within 2.2 m of each other on average with a basic bootstrapped 95% confidence interval (CI) of 0.5 to 3.5 m. Crossovers from airborne IPR thickness focused on the thin ice area and ice shelf terminus (n = 158) agreed to within 3.3 m (CI: 2.7 to 3.9 m), whereas the general NIS survey thickness crossovers (n= 99) agreed within 7.7 m (CI: 5.6 to 9.6 m). Ice thickness in the ground-based IPR survey was 2.1 m thinner on average (n=113) than the airborne survey of the thin ice area with a mean absolute difference of 3.5 m (CI: 2.8 to 4.2 m).

Average surface elevation crossover errors in the ground-based (n=23) and airborne (n=557) IPR surveys were 0.71 m (CI: 0.21 to 1.11 m) and 1.02 m (CI: 0.80 to 1.19 m), respectively. Surface elevation from ground-based surveying was 0.08 m higher on average (CI: -0.10 to 0.23 m) than the airborne elevation (n = 189) with a mean absolute difference of 0.69 m (CI: 0.54 to 0.81 m).

The relative uncertainty in ice shelf draft can be derived from these two errors added in quadrature. For example, NIS basal draft estimations from the ground-based survey have an uncertainty of  $\pm 3.7$  m, 95% of the time, whereas the airborne survey focused on the thin region and terminus has an uncertainty of  $\pm 4.1$  m; the entire airborne survey has an uncertainty of  $\pm 9.7$  m.

## Data availability

Ice penetrating radar data and locations of ~~meltwater~~ Ice Shelf Water from the ocean glider can be found here: 10.5281/zenodo.4891281. Landsat satellite imagery is freely available from USGS (<https://earthexplorer.usgs.gov/>), with REMA, ITS\_LIVE, and GoLIVE data freely available from NSIDC (<https://nsidc.org>). Ice shelf basal melt data is available through UCSD Library Digital Collections.

## Author contribution

CFD and DM developed the project, analysed the radar and satellite data, and undertook the ground-based radar fieldwork. PW processed the radar data and provided initial analyses. DF, ALF, and JM collected, processed, and analysed the ocean glider data. JG and DDB contributed the airborne radar data and assisted with processing and interpretation. CKL and WSL provided field support and contributed to project design. CFD wrote the manuscript with input from all authors.

## Competing interests

The authors declare that they have no conflict of interest.



## Acknowledgements

690 CD was supported by the Natural Sciences and Engineering Research Council of Canada (NSERC; RGPIN-03761-2017) and the Canada Research Chairs Program (950-231237). DM was supported by NSERC (RGPIN-06244-2016), the Canada Foundation for Innovation, the Ontario Research Fund (314190) and a Canadian Arctic-Antarctic exchange Polar Continental Shelf Program (647-17). JSG was supported by NSF OPP-2114454. Airborne radar and ocean glider data were collected by the support of the Korean Ministry of Oceans and Fisheries (KIMST20190361 (PM21020), which also support  
695 W S Lee and C-K Lee. The authors also thank Jin Hong Kim, Laura Lindzey, Enrica Quartini, and Dillon Buhl for assistance in the field. This is UTIG contribution #####. We thank Ala Khazendar and an anonymous reviewer, along with the editor, for their helpful comments on this manuscript.

## References

- 700 Adusumilli, S., Fricker, H. A., Medley, B., Padman, L., and Siegfried, M. R.: Interannual variations in meltwater input to the Southern Ocean from Antarctic ice shelves. *Nat Geosci*, 13(9), 616-620, 2020
- Alley, K. E., Scambos, T. A., Siegfried, M. R., and Fricker, H. A.: Impacts of warm water on Antarctic ice shelf stability through basal channel formation. *Nat Geosci*, 9(4), 290-293, 2016
- [Alley, K.E., Scambos, T.A., Anderson, R.S., Rajaram, H., Pope, A. and Haran, T.M.: Continent-wide estimates of Antarctic strain rates from Landsat 8-derived velocity grids. \*Journal of Glaciology\*, 64\(244\), 321-332, 2018](#)
- 705 Alley, K. E., Scambos, T. A., Alley, R. B. and Holschuh, N.: Troughs developed in ice-stream shear margins precondition ice shelves for ocean-driven breakup. *Science Advances*, 5(10), p.eaax2215, 2019.
- Baroni, C., Frezzotti, M., Giraudi, C., and Orombelli, G.: Ice flow and surficial velocity inferred from satellite image and air photo analysis of Larsen Ice tongue, Hells Gate and Nansen ice shelves (Northern Victoria Land, Antarctica). *Memorie Della Societa'Geologica Italiana*, 46, 69-80. 1991
- 710 [Bassi24asis](#), J.N. and Ma, Y.: Evolution of basal crevasses links ice shelf stability to ocean forcing. *Earth and Planetary Sc Lett*, 409, 203-211. 2015
- Bell, R. E., Chu, W., Kingslake, J., Das, I., Tedesco, M., Tinto, K. J., Zappa C. J., Frezzotti, M., Boghosia, A., and Lee, W. S.: Antarctic ice shelf potentially stabilized by export of meltwater in surface river. *Nature*, 544(7650), 344-348. 2017
- 715 Borstad, C., McGrath, D. and Pope, A.: Fracture propagation and stability of ice shelves governed by ice shelf heterogeneity. *Geophys Res Lett*, 44(9), 4186-4194. 2017
- Bromwich D. H. and Kurtz D. D.: Katabatic wind forcing of the Terra Nova Bay Polynya. *J Geophys Res- Earth*. 89(C3), 3561–3572, doi:10.1029/JC089iC03p03561, 1984.
- Chartrand, A. M. and Howat, I. M.: Basal Channel Evolution on the Getz Ice Shelf, West Antarctica. *J Geophys Res- Earth*, 125(9), p.e2019JF005293, 2020.
- 720 Ciappa, A., Pietranera, L., and Budillon, G.: Observations of the Terra Nova Bay (Antarctica) polynya by MODIS ice surface temperature imagery from 2005 to 2010. *Remote Sens Environ*, 119, 158-172, 2012
- [Das, I., Padman, L., Bell, R.E., Fricker, H.A., Tinto, K.J., Hulbe, C.L., Siddoway, C.S., Dhakal, T., Frearson, N.P., Mosbeux, C. and Cordero, S.I.: Multidecadal basal melt rates and structure of the Ross Ice Shelf, Antarctica, using airborne ice penetrating radar. \*Journal of Geophysical Research: Earth Surface\*, 125\(3\), p.e2019JF005241. 2020](#)
- 725 Dow, C. F., Lee, W. S., Greenbaum, J. S., Greene, C. A., Blankenship, D. D., Poinar, K., Forrest, A., Young, D., and Zappa, C. J.: Basal channels drive active surface hydrology and transverse ice shelf fracture. *Science Advances*, 4(6), eaao7212, 2018.
- Drews, R: Evolution of ice shelf channels in Antarctic ice shelves. *Cryosphere*, 9(3), 1169-1181, 2015.

- 730 Dupont, T. K., and Alley, R. B.: Assessment of the importance of ice-shelf buttressing to ice-sheet flow. *Geophys Res Lett*, 32(4), 2005.
- Dutrieux, P., Vaughan, D. G., Corr, H. F., Jenkins, A., Holland, P. R., Joughin, I., and Fleming, A. H.: Pine Island glacier ice shelf melt distributed at kilometre scales. *Cryosphere*, 7(5), 1543-1555, 2013.
- 735 Fricker, H. A., Popov, S., Allison, I., & Young, N.: Distribution of marine ice beneath the Amery Ice Shelf. *Geophys Res Lett*, 28(11), 2241-2244, 2001.
- [Friedrichs, D.M., McInerney, J.B., Oldroyd, H.J., Lee, W.S., Yun, S., Yoon, S.T., Stevens, C.L., Zappa, C.J., Dow, C.F., Mueller, D. and Sepúlveda Steiner, O.: Observations of submesoscale eddy-driven heat transport at an ice shelf calving front. \*Communications Earth & Environment\*, 3\(1\), p.140. 2022.](#)
- 740 Fujita, S., Matsuoka, T., Ishida, T., Matsuoka, K., and Mae, S: A summary of the complex dielectric permittivity of ice in the megahertz range and its applications for radar sounding of polar ice sheets. In *Physics of Ice Core Records* (p. 185-212). Hokkaido University Press, 2000.
- Fürst, J. J., Durand, G., Gillet-Chaulet, F., Tavard, L., Rankl, M., Braun, M. and Gagliardini, O.: The safety band of Antarctic ice shelves. *Nat Clim Change*, 6(5), 479-482, 2016.
- 745 Gardner, A. S., Fahnestock, M. A. and Scambos T. A.: MEaSURES ITS\_LIVE Landsat Image-Pair Glacier and Ice Sheet Surface Velocities: Version 1, 2020.
- Gladish, C. V., Holland, D. M., Holland, P. R., and Price, S. F.: Ice shelf basal channels in a coupled ice/ocean model. *J Glaciol*, 58(212), 1227-1244, 2012.
- 750 Goldberg, D. N., Gourmelen, N., Kimura, S., Millan, R. and Snow, K.: How accurately should we model ice shelf melt rates? *Geophys Res Lett*, 46(1), 189-199, 2019.
- Greene, C. Antarctic geoid conversions (<https://www.mathworks.com/matlabcentral/fileexchange/54104-antarctic-geoid-conversions>), MATLAB Central File Exchange. Retrieved June 2, 2021.
- Holland P. R., Corr H. F., Vaughan D. G., Jenkins A, and Skvarca P: Marine ice in Larsen Ice Shelf. *Geophys Res Lett*, 36(11), 2009.
- 755 Howat I. M, Porter C, Smith B. E., Noh M. J. and Morin P.: The Reference Elevation Model of Antarctica. *Cryosphere* 13, 665–674, doi:10.5194/tc-13-665-2019, 2019.
- Hulbe, C.L., LeDoux, C. and Cruikshank, K.: Propagation of long fractures in the Ronne Ice Shelf, Antarctica, investigated using a numerical model of fracture propagation. *J Glaciol*, 56(197), 459-472. 2010.
- 760 Indrigo, C., Dow, C.F., Greenbaum, J.S., and Morlighem, M.: Drygalski Ice Tongue stability influenced by rift formation and ice morphology. *J Glaciol*, doi.org/10.1017/jog.2020.99, 2021.
- [Jordan, J. R., Holland, P. R., Jenkins, A., Piggott, M. D., and Kimura, S.: Modeling ice-ocean interaction in ice-shelf crevasses, \*J. Geophys. Res. Oceans\*, 119, 995– 1008, doi:10.1002/2013JC009208, 2014](#)
- 765 Khazendar, A., Tison, J.L., Stenni, B., Dini, M. and Bondesan, A.: Significant marine-ice accumulation in the ablation zone beneath an Antarctic ice shelf. *J Glaciol*, 47(158), 359-368, 2001.
- [Khazendar, A., and A. Jenkins: A model of marine ice formation within Antarctic ice shelf rifts, \*J. Geophys. Res.\*, 108\(C7\), 3235, doi:10.1029/2002JC001673, 2001](#)
- Kulesa, B., Jansen, D., Luckman, A. J., King, E. C., and Sammonds, P. R. Marine-ice regulates the future stability of a large Antarctic ice shelf. *Nat Commun*, 5, 3707, 2014.
- 770 Kurtz, D. D., and Bromwich, D. H. Satellite observed behavior of the Terra Nova Bay polynya. *J Geophys Res - Oceans*, 88(C14), 9717-9722, 1983.
- Lipovsky B.: Ice shelf rift propagation and the mechanics of wave-induced fracture. *J Geophys Res – Oceans*, 123, 4014–4033, doi:10.1029/2017JC013664, 2018.

- 775 Lindzey, L. E., Beem, L. H., Young, D. A., Quartini, E., Blankenship, D. D., Lee, C. K., Lee, W. S., Lee, J. I., and Lee, J.: Aerogeophysical characterization of an active subglacial lake system in the David Glacier catchment, Antarctica. *Cryosphere*, 14(7), 2217-2233, 2020.
- Little, C.M., Gnanadesikan, A. and Oppenheimer, M.: How ice shelf morphology controls basal melting. *J Geophys Res - Oceans*, 114(C12), 2009.
- 780 Mankoff, K. D., Jacobs, S. S., Tulaczyk, S. M., and Stammerjohn, S. E.: The role of Pine Island Glacier ice shelf basal channels in deep-water upwelling, polynyas and ocean circulation in Pine Island Bay, Antarctica. *Ann Glaciol*, 53(60), 123-128, 2012.
- Manzella, G. M. R., Meloni, R., and Picco, P.: Current, temperature and salinity observations in the Terra Nova Bay polynya area. In *Oceanography of the Ross Sea Antarctica* (pp. 165-173). Springer, Milano, 1999.
- 785 Mingo, L. and Flowers, G.E.: An integrated lightweight ice-penetrating radar system. *J Glaciol*, 56(198), 709-714, 2010.
- McGrath, D., Steffen, K., Scambos, T., Rajaram, H., Casassa, G. and Lajos, J.L.R., 2012. Basal crevasses and associated surface crevassing on the Larsen C ice shelf, Antarctica, and their role in ice-shelf instability. *Ann Glaciol*, 53(60), 10-18. 2012
- 790 [McGrath, D., Steffen, K., Holland, P. R., Scambos, T., Rajaram, H., Abdalati, W., and Rignot, E.: The structure and effect of suture zones in the Larsen C Ice Shelf, Antarctica, \*J. Geophys. Res. Earth Surf.\*, 119, 588– 602, doi:10.1002/2013JF002935. 2014](#)
- Moore, J. C., Reid, A. P., and Kipfstuhl, J.: Microstructure and electrical properties of marine-ice and its relationship to meteoric ice and sea ice. *J Geophys Res - Oceans*, 99(C3), 5171-5180, 1994.
- 795 Morlighem, M. MEaSURES BedMachine Antarctica, Version 2. Boulder, Colorado USA. NASA National Snow and Ice Data Center Distributed Active Archive Center. 2020.
- Mouginot, J., B. Scheuchl, and E. Rignot.: MEaSURES Antarctic Boundaries for IPY 2007-2009 from Satellite Radar, Version 2. Boulder, Colorado USA. NASA National Snow and Ice Data Center Distributed Active Archive Center. doi:10.5067/AXE4121732AD, 2017.
- 800 [Neckel, N., Drews, R., Rack, W. and Steinhage, D.: Basal melting at the Ekström Ice Shelf, Antarctica, estimated from mass flux divergence. \*Annals of Glaciology\*, 53\(60\), pp.294-302. 2012](#)
- 805 Nicholls, K. W., Abrahamsen, E. P., Buck, J. J. H., Dodd, P. A., Goldblatt, C., Griffiths, G., Heywood, K. J., Hughes, N. E., Kaletzký, A., Lane-Serff, G. F. and McPhail, S. D.: Measurements beneath an Antarctic ice shelf using an autonomous underwater vehicle. *Geophys Res Lett*, 33(8). 2006
- Raymond, M. J. and Gudmundsson, G. H. On the relationship between surface and basal properties on glaciers, ice sheets, and ice streams. *J Geophys Res - Solid Earth*, 110(B8), 2005. Rusciano, E., Budillon, G., Fusco, G., and Spezie, G.: Evidence of atmosphere–sea ice–ocean coupling in the Terra Nova Bay polynya (Ross Sea—Antarctica), *Cont Shelf Res*, 61–62, 112–124, doi:10.1016/j.csr.2013.04.002, 2013
- 810 Scambos, T. A., Berthier, E., Haran, T., Shuman, C. A., Cook, A. J., Ligtenberg, S., and Bohlander, J.: Detailed ice loss pattern in the northern Antarctic Peninsula: widespread decline driven by ice front retreats. *Cryosphere*, 8(6), 2135-2145, 2014.
- Scambos, T., Fahnestock, M., Moon, T., Gardner, A., and Klinger, M.: Global Land Ice Velocity Extraction from Landsat 8 (GoLIVE), Version 1. Boulder, Colorado USA. NSIDC: National Snow and Ice Data Center. doi:10.7265/N5ZP442B, 2016.
- 815 Stevens, C., Lee, W. S., Fusco, G., Yun, S., Grant, B., Robinson, N., and Hwang, C. Y.: The influence of the Drygalski Ice Tongue on the local ocean. *Ann Glaciol*, 58(74), 1–9, doi:10.1017/aog.2017.4, 2017.
- Stevens, C., Hulbe, C., Brewer, M., Stewart, C., Robinson, N., Ohneiser, C. and Jendersie, S.: Ocean mixing and heat transport processes observed under the Ross Ice Shelf control its basal melting. *P Natl Acad Sci*, 117(29), 16799-16804, 2020.
- 820 Tison, J. L., Khazendar, A. and Roulin, E.: A two-phase approach to the simulation of the combined isotope/salinity signal of marine ice. *J Geophys Res - Oceans*, 106(C12), 31387-31401, 2001

Wei, W., Blankenship, D. D., Greenbaum, J. S., Gourmelen, N., Dow, C. F., Richter, T. G., ... and Assmann, K. M.: Getz Ice Shelf melt enhanced by freshwater discharge from beneath the West Antarctic Ice Sheet. *Cryosphere*, 14(4), 1399-1408, 2020.

825 Weertman, J. Can a water-filled crevasse reach the bottom surface of a glacier. *International Association of Hydrological Sciences*, 95, 139-145, 1973.

Vaughan, D. G., Corr, H. F., Bindschadler, R. A., Dutrieux, P., Gudmundsson, G. H., Jenkins, A., Newman, T., Vornberger, P., and Wingham, D. J.: Subglacial melt channels and fracture in the floating part of Pine Island Glacier, Antarctica. *J Geophys Res - Earth*, 117(F3), 2012.

830